Core-scale geophysical and hydromechanical analysis of seabed sediments affected by CO_2 venting

By

Ismael Himar Falcon-Suarez[1]*; Anna Lichtschlag[1]; Hector Marin-Moreno[3]; Giorgos Papageorgiou[4,5]; Sourav K. Sahoo[1]; Ben Roche[2]; Ben Callow[2]; Romina A.S. Gehrmann[2]; Mark Chapman[4] & Laurence North[1]

1. National Oceanography Centre, University of Southampton Waterfront Campus. European Way, SO14 3ZH, Southampton, UK.
2. School of Ocean and Earth Science, National Oceanography Centre Southampton, University of Southampton Waterfront Campus, European Way, Southampton SO14 3ZH, UK.
3. Norwegian Geotechnical Institute, PB 3930 Ullevål Stadion, NO-08906 Oslo, Norway.
4. School of Geosciences, University of Edinburgh, Grant Institute, West Mains road, Edinburgh EH9 3FE, UK.
5. Institute of Geoscience and Petroleum, NTNU, S. P. Andersensvei 15A, 7491, Trondheim, Norway.

*Corresponding author: National Oceanography Centre, University of Southampton Waterfront Campus. European Way, SO14 3ZH, Southampton.
Phone: +44 (0)23 8059 6666 Office: 676/07 email: isfalc@noc.ac.uk

Abstract

Safe offshore Carbon Capture Utilization and Storage (CCUS) includes monitoring of the subseafloor, to identify and assess potential CO_2 leaks from the geological reservoir through seal bypass structures. We simulated CO_2-leaking through shallow marine sediments of the North Sea, using two gravity core samples from ~1 and ~2.1 meters below seafloor. Both samples were subjected to brine-CO_2 flow-through, with continuous monitoring of their transport, elastic and mechanical properties, using electrical resistivity, permeability, P-wave velocity and attenuation, and axial strains. We used the collected geophysical data to calibrate a resistivity-saturation model based on Archie's law extended for clay content, and a rock physics for the elastic properties. The P-wave attributes detected the presence of CO_2 in the sediment, but failed in providing accurate estimates of the CO_2 saturation. Our results estimate porosities of 0.44 and 0.54, a background permeability of ~10^{-15} and ~10^{-17} m^2, and maximum CO_2 saturation of 18% and 10% (±5%), for the sandier (shallower) and muddier (deeper) sample, respectively. The finer-grained sample likely suffered some degree of gas-induced fracturing, exhibiting an effective CO_2 permeability increase sharper than the coarser-grained sample. Our core-scale multidisciplinary experiment contributes to improve the general interpretation of shallow sub-seafloor gas distribution and migration patterns.

Key words: elastic waves, electrical resistivity, marine sediments, CO_2 storage

1. Introduction

Carbon Capture Utilization and Storage (CCUS) is a realistic global scale mitigation solution to tackle the excess of CO_2 expelled from industrial production and sequestering it into deep reservoir formations. CO_2 sequestration activities encompasses pre-injection risk assessment about sealing efficiency and mechanical stability of the reservoir, and CO_2 plume migration monitoring during and after CO_2 injection (EU CCS Directive, 2009).

In case of seal failure, the way the CO_2 reaches shallower areas depends on a number of factors, including the porosity and permeability of the overburden formations; sediment heterogeneity and grain size distribution; vertical hydraulic connectivity between layers through existing and induced sedimentary seal bypass systems (Cartwright et al., 2007), such us faults (e.g., Rutqvist, 2012) or chimney structures (e.g., Bull et al., 2018; Karstens and Berndt, 2015; Robinson et al., 2021); and the reactivity of these materials to CO_2 (e.g., Marín-Moreno et al., 2019).

Offshore, gas-escape expressions include seabed depressions known as pockmarks (e.g., Robinson et al., 2021). Most of them are only 2 - 3 m in diameter (Bull et al., 2018), fed by sub-seismic scale structures located at the shallowest part of the sediment column, or by deeper and larger chimney structures with the potential of connecting reservoirs with the seabed (Bull et al., 2018). Hence, the understanding of the hydrodynamic behaviour of sediments prior to venting and pockmark formation is crucial to improve monitoring tools and interpretation of seal bypass systems underground.

In offshore CCUS sites, once the CO_2 reached the seafloor, the detection and quantification of the leak can be done using physicochemical sensors measuring in the water column (e.g., Blackford et al., 2015). However, to minimize the risk of

leakage, and for commercial global CO_2 storage operations to become realistic, monitoring CO_2 migration through the sediment column is essential. This is particularly challenging in offshore storage sites, as the deployment of equipment and monitoring require advanced technology (e.g., Robinson et al., 2021). Therefore, understanding the sub-seafloor CO_2 migration patterns is of great importance to inform about best offshore sensors deployment locations, which is critical for setting up the risk assessment for the CCUS complex.

Unlike the sensors used to detect and quantify dissolved CO_2 concentrations and bubbles directly in the water column, inferring the presence of CO_2 below the seafloor requires advanced remote sensing tools. The increase of free gas in the sediment leads to detectable geophysical signatures, as the bulk physical properties of the sediment change. For this reason, active seismic and electromagnetic methods (historically used in reservoir exploration) are the most widespread techniques for CO_2 storage monitoring (e.g., Chadwick et al., 2019; Park et al., 2017). Seismic surveys provide information about the bulk elastic properties of both the mineral skeleton and the pore fluid; electrical datasets complement the seismic interpretation with further complementary information about structure of the porous medium and the fluid(s) distribution therein (e.g., Mavko et al., 2009). Therefore, joint elastic-electrical datasets are powerful tools for reservoir interpretation.

The development of robust tools to identify and interpret the geophysical signatures corresponding to real cases of CO_2 migration from reservoirs through the overburden requires datasets generated from controlled experiments under *in situ* conditions. Field scale physical simulations are challenging, and include pilot site testing (e.g., Michael et al., 2010; Underschultz et al., 2011; Würdemann et al., 2010), and *in situ* release experiments (e.g., Dean et al., 2020; Flohr et al., 2021;

98 Taylor et al., 2015). Additionally, rock physics flow-through laboratory experiments
99 enable to study the behaviour of CO_2 propagation in (water/brine) saturated porous
100 media in a more controlled manner (Burnside and Naylor, 2014), providing joint
101 elastic-electrical datasets when acoustic and electrical sensors are available (e.g.,
102 Alemu et al., 2013; Falcon-Suarez et al., 2017; Kim et al., 2013; Zemke et al., 2010).
103 It is well-known that core-scale laboratory experiments may not be fully
104 representative of the events occurring at field scale. However, they allow the study of
105 specific phenomena to calibrate and improve the understanding of natural processes
106 and interpretation of field scale datasets.

107 Most of the multiphase-flow laboratory tests for studying elastic and electrical
108 properties of CO_2–bearing porous media focus on the study of the host and sealing
109 formations at CCUS reservoir conditions (generally located at depths greater than
110 1000 m below seabed). The experimental research of sediments partially saturated
111 with free gas in the shallower part of the sediment column (i.e., the near seafloor
112 sediments) requires a combined petrographic, hydrological, geomechanical and
113 geotechnical approach to complement geophysical data for interpreting seafloor
114 dynamics (e.g., Blouin et al., 2019; Deusner, 2016). But, simulating shallow
115 conditions in the laboratory is challenging. Close to seafloor, the effective stress is
116 low and any increase in pore pressure, e.g., due to the expansion of CO_2 while
117 moving upwards, may affect seafloor stability. Replicating these circumstances in the
118 laboratory requires a precise control of the state of stress and adequate sensors to
119 enable the study of the CO_2–induced hydromechanical effects on the shallower part
120 of the sedimentary column. In May 2019, a controlled *in situ* CO_2-release experiment
121 was conducted in the North Sea (Flohr et al., 2021), funded by the Horizon 2020
122 project Strategies for Environmental Monitoring of Marine Carbon Capture and

Storage (STEMM-CCS). STEMM-CCS was a multidisciplinary project that aimed to enhance the marine monitoring of CCUS activities to assess the environmental impacts associated with potential CO_2 leaks from the geological reservoir (Dean et al., 2020). A complementary project funded by NERC UK entitled Characterization of Major Overburden Leakage Pathways above Sub-seafloor CO_2 Storage Reservoirs in the North Sea (CHIMNEY (Bull et al., 2018)), focused on improving the understanding of subsurface fluid pathways, and developing tools to identify seal bypass systems and quantify partial gas saturation. During both STEMM-CCS and CHIMNEY several geophysical surveys were carried out in the North Sea (Achterberg and Esposito, 2018; Böttner et al., 2020; Gehrmann et al., 2021; Karstens et al., 2019), including seismic and electromagnetic data acquisition. These geophysical data which together with *in situ* samples and modelling result in a comprehensive amount of information about the shallower part of the sediment column (Robinson et al., 2021).

In this work, we assess the results obtained from laboratory brine-CO_2 flow-through tests with geophysical monitoring, using sediment core samples collected in the vicinity of the Goldeneye platform (Achterberg and Esposito, 2018), nearby the STEMM-CCS CO_2 release experiment site. The aim of the lab tests was to relate geophysical changes in the first 3 metres below seafloor (mbsf) to the observed hydromechanical evolution during the CO_2 injection. Our results contribute to calibrate subseafloor geophysical data collected during the STEMM-CCS CO_2 release experiment and help improve future interpretations of shallow sub-seafloor CO_2 distribution and migration patterns.

2. Methodology

2.1. Core samples information

Gravity core POS527-GC06 was collected prior to the *in situ* CO_2 release experiment close to the experimental release site in the UK sector of the North Sea (POS527 Station 102, latitude, 57 59.734; longitude, 0 22.383 (Achterberg and Esposito, 2018)), containing sediments of the Witch Ground Formation (e.g., Böttner et al., 2020; Roche et al., 2021). Standard international procedures (IODP - international gold standard core curation) were followed to maintain the integrity and minimise water loss of the sediment. The core was cut in 1 m sections and whole rounds were scanned with a multi-sensor core logger (MSCL) at the British Ocean Sediment Core Research Facility (BOSCORF).The MSCL analysis included P-wave velocity (at frequency of 230 kHz), electrical resistivity, bulk density and porosity estimates. After the MSCL analysis the cores sections were split. To preserve the original saturation, the two halves of each core section were wrapped in food grade cling film (and stored at 4° C), which is commonly used as a multilayer barrier film in the food industry. The film has excellent minimal water vapour and oxygen transmission rates, and is transparent making it ideal for core preservation. The grain size of the sediment was determined with a Malvern grain size analyser every 20 cm, and then computed with the program Gradistat (Blott and Pye, 2001), allowing the distinction between sand (grain sizes from 63 – 2,000 μm) and silt (grain sizes from 2 – 63 μm) fractions, expressed in terms of sand:mud ratio in Figure 1. Core permeability was estimated using Hazen's modified and Kozeny-Carman's approximations based on the grain-size percentile 10 (d_{10}), using the equations presented in Rosas et al. (2014) and the fitting parameter β recommended by the same authors for offshore siliciclastic sediments. The inorganic carbon carbonate

content of the samples was determined before and after the tests with a ThermoFisher Scientific Flash 2000 Elemental Analyser (EA) by subtracting the organic carbon content, which was measured after the removal of the inorganic carbon with acid, from the total carbon content.

Based on the geophysical and geochemical results (Figure 1), two sample intervals were selected from the core at ~1 and ~2.1 mbsf (hereafter named as samples S-A and S-B, respectively). Samples S-A and S-B were extracted from visually homogeneous areas, weakly laminated, with largest difference in physical properties, and therefore good candidates to study the geophysical variability range in the near-seabed sediments of this part of the Central North Sea. From each interval, a 2 cm length, 5 cm diameter core plug was extracted for this experiment: First, we extracted a ~7 cm subsample of the gravity core sediment from a selected (visually undisturbed) area; then, we drove vertically (along the core axis) a 2 cm length, 5 cm (inner diameter) annulus-wedged mould into the subsample to obtain the test sample plug. The mineralogical composition of the samples was obtained by X-ray diffraction (XRD) with a Philips X'Pert pro XRD-Cu X-ray tube, from trimmings of the gravity core at the sample depths (Table 1). The physical properties of the sediment were changing with depth from sand-dominated at the sediment surface to mud-dominated below 3 mbsf. The two selected samples had a distinctly different grain size (with sand:mud ratio of ~40:60 for sample S-A, and ~25:75 for S-B; Figure 1), and porosities of 0.44 ±0.01, for sample S-A (sandier), and 0.54 ±0.01, for S-B(muddier), with permeabilities (from grain size) in the order of 10^{-14} and 10^{-15} m^2, respectively. Porosities were estimated from core trimmings (collected nearby the samples) using wet-(60° C oven) dry mass balance from well-known soil volume portions, with the estimates being in good agreement with the MSCL data (Figure 1).

The inorganic carbon content was slightly lower in the shallower (1.4 ± 0.3 wt% for S-A) than in the deeper (1.5 ± 0.3 wt% for S-B) sample.

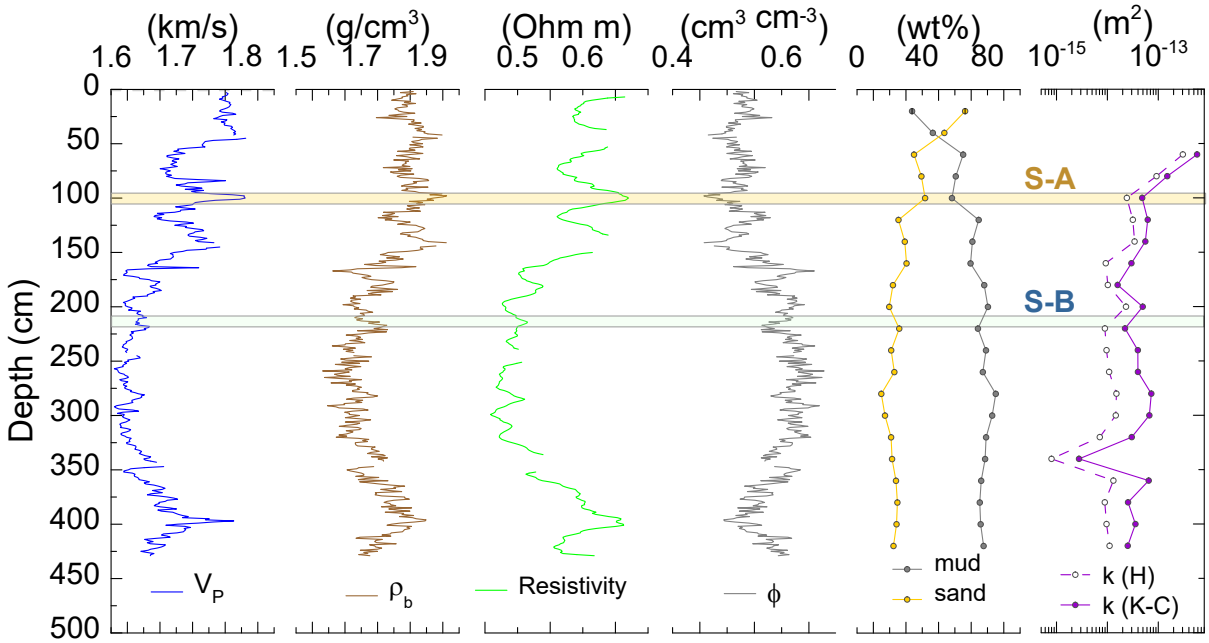

Figure 1. P-wave velocity (V_P at 230 kHz), bulk density (ρ_b), resistivity and porosity (ϕ) obtained from multi-sensor core logger (MSCL at BOSCORF, NOC) analysis along the core POS527-06 (measurements taken every 1 cm depth), estimates of grain size from sampling (in class weight %, every 20 cm depth) and permeability (k) estimates based on grain size percentile 10 using Hazen's (H) and Kozeny-Carman's (K-C) approximations (e.g., Rosas et al., 2014). Marked depths for samples S-A (yellow) and S-B (green).

Table 1. Mineralogical composition (wt%) of the gravity core POS527-GC06, at samples S-A and S-B depths

Depth (cm)	Calcite	Dolomite	Orthoclase	Plagioclase	Quartz	Chlorite	Mica
100	2.7	1.6	6.3	9.9	67.2	5.2	7.1
210	4.3	1.3	8.8	9.9	56.2	6.7	12.7

2.2. Experimental setup

For each sample (S-A and S-B), we performed a brine-CO_2 flow-through test with geophysical and hydromechanical monitoring. The tests were conducted using

211 the high pressure room-temperature (20º C) experimental setup for multiflow-through
212 tests at the National Oceanography Centre, Southampton (NOC) (Falcon-Suarez et
213 al., 2017).
214 The experimental rig was set up in a multi-flow configuration under well-
215 controlled flow, and confining and pore pressure conditions (ISCO-pumping
216 controllers). We imposed hydrostatic confining conditions of stress for this
217 experiment (i.e., $\sigma_1 = \sigma_2 = \sigma_3$). To minimize fluid-induced corrosiveness effects on
218 the equipment, we use fluid transfer vessels (FTVs) for storing and
219 delivering/receiving the pore fluids. Here, two FTVs were used for delivering brine
220 and CO_2, and a third one for receiving the pore fluid downstream. The rig
221 implements sensors for measuring, simultaneously, ultrasonic P- and S-waves
222 attributes (velocity and attenuation), electrical resistivity and axial strains. Only the
223 ultrasonic sensor for P-wave (transmitting 400 to 1,000 kHz broadband acoustic
224 pulses (Falcon-Suarez et al., 2020b)) provided a reliable signal during this
225 experiment. The sensor is housed in one of the two platens that axially confine the
226 sample through a polyether ether ketone (PEEK) buffer rods. These rods have well-
227 defined acoustic impedance and low energy loss, and provide a delay path with clear
228 top/base sample reflections from which the ultrasonic P-wave velocity (precision ±
229 0.1%; accuracy ± 0.3%) and attenuation (accuracy ± 5%) are calculated, using the
230 pulse-echo technique (Best, 1992; Falcon-Suarez et al., 2020b). From the axial
231 platens, two arms hold linear variable differential transformer (LVDT) sensors for
232 axial strain monitoring.
233 Inside the triaxial vessel, an array of 16 stainless steel electrodes are imbibed
234 in the rubber sleeve that isolates the rock sample from the confining mineral oil.
235 Once in contact with the sample, the bulk electrical resistivity is measured using an

236 electrical resistivity tomography (ERT) data acquisition system designed and
237 developed at the NOC (North et al., 2013). The system uses a tetra-polar electrode
238 configuration to minimize electrode polarization artefacts. For any single operational
239 run, the ERT system acquires 208 individual tetra-polar measurements using various
240 permutations of current injection and potential difference sensing electrode pairs.
241 The collected data are then inverted using software based upon EIDORS (Adler and
242 Lionheart, 2006) MATLAB toolkit for both a uniform/homogeneous isotropic resistivity
243 and a heterogeneous isotropic resistivity distribution. Under our experimental P-T-
244 fluid salinity conditions, the error of the resulting resistivity is <1% for homogenous
245 and isotropic porous media with bulk electrical resistivity <100 Ω m (i.e., for the fully
246 saturated, single brine flow stages). Estimation of errors for inhomogeneous and
247 anisotropic resistivity distributions is a non-trivial problem. Indeed, for the case of
248 anisotropic materials no unique solution exists for a resistivity distribution within a
249 body determined from potential measurements made on its surface (Kohn and
250 Vogelius, 1984). Hence, the presence of anisotropy may cause significant errors in
251 resistivity determination. Furthermore the resistivity inverse problem is ill-posed and
252 significant smoothing is usually applied to solution (in this case via a Tikhonov
253 penalty function) to enable solution convergence of the data inversion process. Thus
254 the NOC RPL tomography system is able to detect gross heterogeneity in the
255 internal resistivity distribution of the sample on the order of a centimetre. Also, small
256 high resistivity contrast heterogeneities, for example fractures, are blurred and do not
257 possess sharp boundaries in the interpreted ERT images. Thus while our system
258 can indicate the presence of heterogeneity and or anisotropy its main purpose is to
259 enable the degree of heterogeneity to be assessed. This is useful as ideally one
260 desires the sample to be a representative elementary volume and, therefore,

homogeneous (further details about data processing and calibration in North et al. (2013) and North and Best (2014)).

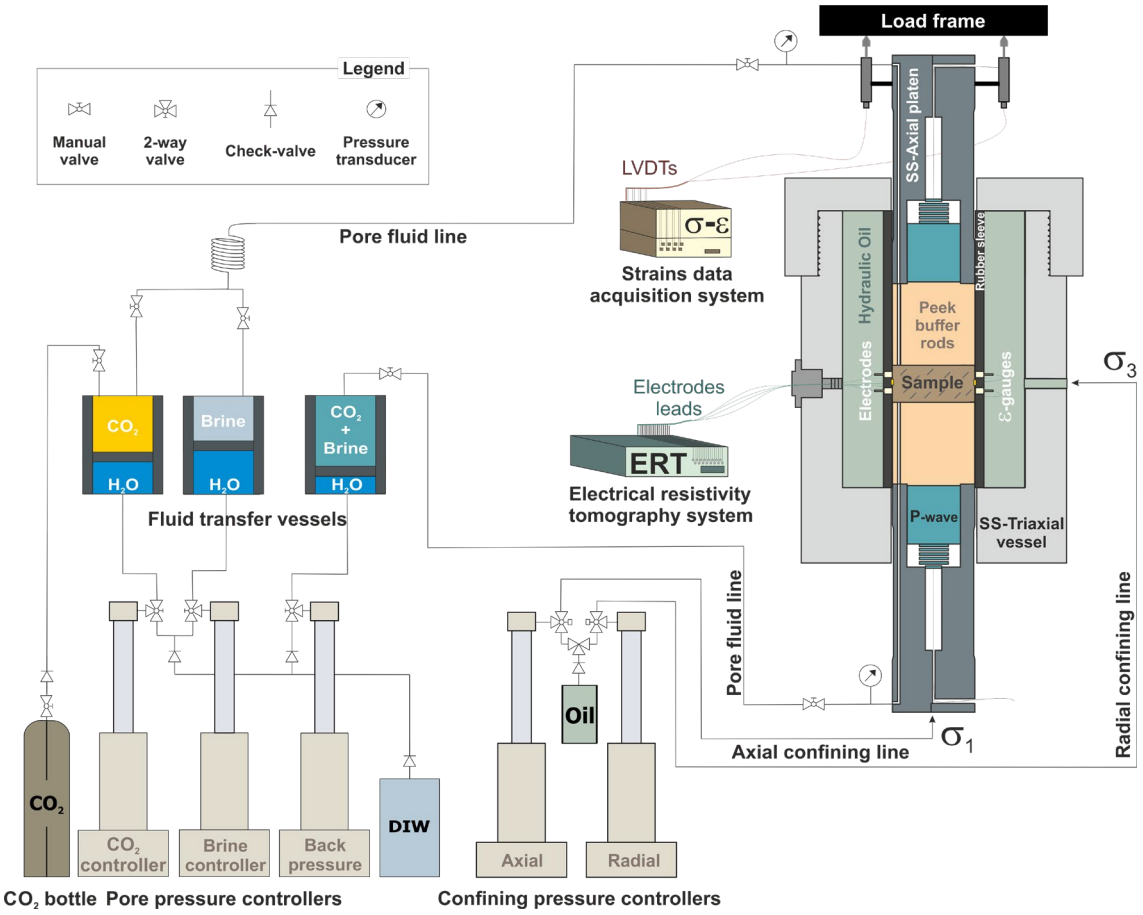

Figure 2. Experimental rig for multi-flow tests at the National Oceanography Centre (NOC), Southampton.

2.3. Brine and CO_2 flow-through (BCFT) tests

The samples are poorely-consolidated and required a careful and special preparation to fit into the triaxial cell of the experimental rig (Figure 2), originally designed to host rock plugs. Originally, we assumed that the samples were still fully saturated in the original seawater brine when tested. This assumption was supported by a posteriori mass balance calculation.

The following procedure was applied to both samples prior to testing:

Firstly, with the sample still placed in the annulus-wedged mould, it was sandwiched by two annuli (PEEK) holding nylon-tight membranes (common pore size < 2 μm), acting as sieves to counteract the unconsolidated state of the sample. This configuration minimizes pipe clogging due to grain migration, and ensures an appropriate top/base repartition of the axial loading (Falcon-Suarez et al., 2018). Also, once the radial stress is slightly increased, the smooth-wall of the two PEEK-annuli in contact with the internal sleeve minimizes potential fluid migration along the sample-sleeve contact.

Secondly, the sample was smoothly removed from the wedge-annulus directly onto the axial platen upstream, and then altogether placed in the triaxial cell core holder at room temperature (20° C). Note that the upstream reservoir (i.e., inlet pipe network) was previously saturated with the testing brine to remove any air in the pipes up to the inlet port. Downstream, the reservoir is left open to remove the air by a continuous brine flow-through upwards, at minimum confining pressure (P_c) of 0.2 MPa.

Thirdly, once the fluid was observed at the outlet port, the hydraulic system was closed and both the confining (P_c) and pore pressure (P_p) were simultaneously increased up to P_c ~1.4 MPa and P_p ~1.2 MPa, the target conditions estimated for the sediments above the STEMM-CCS CO_2-release test site (i.e., 3 mbsf at 120 m water depth (Flohr et al., 2021). Then, the sample was left for no less than 24 h in the triaxial vessel to settle, while subjected to brine flood under minimum flow rate (0.01 mL/min) to enable the testing brine (synthetic 3.5% NaCl aqueous solution, with density 1023.9 kg m^{-3} at the experimental PT conditions) to replace the parental pore fluid.

298 Our tests combined two consecutive flow-through stages each, consisting of (i)
299 single brine flow and (ii) CO_2 flow-through the brine saturated sample. During the
300 first stage, brine was flushed through the samples and the permeability was
301 calculated using Darcy's law (see below), with slightly variable conditions of effective
302 pressure ($P_{eff} = P_c - P_p$) to assess also the stress-sensitivity of the permeability. For
303 this stage, the system was configured in control pressure mode to avoid negative P_{eff}
304 and development of preferential path-flows, which cause misleading permeability
305 results. In the second stage, the brine saturated sample was flushed with CO_2 (in
306 gas state at the experimental PT conditions, with density 25.6 kg m^{-3}) at increasing
307 flow rates (0.07, 0.18, 0.37, 0.55, 0.74 kg d^{-1}), to investigate the geophysical
308 signatures associated with CO_2-induced hydromechanical changes. With this
309 methodology, we aimed to reproduce an increasing level of hydraulic pressure within
310 the sediment column, similarly to the test procedure used for the STEMM-CCS CO_2
311 release experiment (Flohr et al., 2021), but under controlled conditions, and at
312 reduced spatial and temporal scale and hydraulic energy.
313 At the end of the tests, gradually, both P_c and P_p were slowly (~1 h) decreased
314 keeping P_{eff} constant. This procedure minimizes the brine displacement due to CO_2
315 decompression and gas exolution, in turn, allows a rough estimate (here taken only
316 qualitatively; see below) of the final degree of brine saturation in the sample by mass
317 balance.

318 *2.4. Effective permeability*

319 When more than one fluid is moving through a porous medium, the (effective)
320 permeability of each fluid is different. Our samples are muddy sediments that, under
321 the drainage conditions of our tests, present resistance to gas flow. This resistance
322 is determined by the breakthrough capillary pressure, which is controlled by grain

size and pore throats distribution, the properties of the fluids and the flow conditions (Dullien, 1992). . Once the pore pressure exceeds this resistance and the non-wetting phase percolates, the leakage rate (Q_{out}) under laminar (Darcy's flow) conditions is controlled by the effective permeability (k_{eff}) of the system to the breaking fluid flow (CO_2 in our case), as follows:

$$Q_{out} = \frac{A \Delta P_P k_{eff}}{L \mu_{CO2}}, \quad (1)$$

where A and L are area and length of the sample, ΔP_P is the (up- and downstream) pore pressure gradient and μ_{CO2} is the dynamic viscosity of the penetrating fluid (μ_{CO2} = 1.48 x 10^{-5} Pa s^{-1}, at the experimental conditions, i.e., 20 °C and 1.2 MPa). Note that during the first stage of the tests, brine was the only fluid flowing through the sample. Thus, replacing μ_{CO2} by μ_{brine} (1.52 x 10^{-3} Pa s^{-1}, at the experimental conditions) in Eq. (1), k_{eff} provides the absolute permeability to brine (i.e., Darcy's law).

When the two fluids are present in the porous medium, k_{eff} expresses the CO_2 flow-induced (absolute) permeability (k) reduction through the relative permeability to CO_2 ($k_{r,CO2}$) as $k_{eff} = k \; x \; k_{r,CO2}$, with $k_{r,CO2} \in [0, 1]$. $k_{r,CO2}$, and therefore k_{eff}, increases with the partial saturation of CO_2 (i.e., the inverse of brine saturation: $S_{CO2} = 1 - S_w$). Here, we estimate k_{eff} evolution of the two samples during CO_2 flow-through, assuming steady state conditions on the basis of $Q_{in} = Q_{out}$, ΔP_p = constant, and less than 5% variation between two consecutive bulk resistivity measurements (i.e., below resistivity error). However, our k_{eff} estimates provide only apparent values of $k_{r,CO2}$, as we neglected the calculation of the capillary pressure that should be discounted to the experimental value (e.g., Zhang et al., 2017). Our experimental setup is limited to samples with small length-to-diameter factor (~0.4), which leads to

346 uncertainties in terms of pore fluid distribution across the plug due to capillary end
347 effects, affecting the experimental estimate of the capillary pressure. Although the
348 outlet ports have been designed to minimize this effect, we can still expect
349 underestimations of up to one order of magnitude in relative permeability cross-point
350 and 5-10% in saturation (Muñoz-Ibáñez et al., 2019).

351 *2.5. Resistivity into CO_2 saturation*

352 The bulk electrical resistivity increases with the increasing CO_2 content, but
353 also the error associated to the non-uniform distribution of the gas. We use one
354 unique bulk resistivity value for the whole sample to calculate the bulk degree of
355 saturation, adopting the a conservative error of 5% (for the resistivity variability range
356 measured during the experiment (North et al., 2013); see below), for all the values
357 collected after CO_2 injection. The electrical tomography is used to complement our
358 observations with information about the gas distribution patterns.

359 Resistivity can be transformed into degree of saturation combining Archie's
360 relationships (Archie, 1942) for fully (Eq. (2))and partially saturated (Eq. (3))
361 granular materials:

$$R_0 = R_w \phi^{-m} \quad (2)$$

362 and

$$R_b = R_w S_w^{-n} a \phi^{-m}, \quad (3)$$

363 where R is the electrical resistivity, with the subscripts w for the wet (brine) pore fluid,
364 and 0 and b the bulk resistivity of the rock fully and partially saturated, respectively, a
365 is an empirical parameter commonly close to unity, ϕ is the porosity fraction
366 contributing to the sample conductivity (net porosity for our unconsolidated none
367 cemented samples), and m the cementation exponent. S_w is the degree of brine

saturation, with n being the saturation exponent. The saturation exponent depends on the fluid mixture, with accepted values of ~2 for CO_2-brine systems (e.g., Mavko et al., 2009). The cementation exponent of granular seabed sediments varies with the consolidation and fabric, increasing from 1.5 to 1.9 with decreasing grain sphericity and increasing porosity above 0.4 (Jackson et al., 1978) .Combining Eq. (2) and Eq. (3), we can simplify $S_w = (R_o/R_b)^{1/n}$, for a mechanically and chemically invariable porous media.

Archie's relationship is empirical and was initially found valid for clean (shale-free) sandstones. The presence of a shale fraction in the porous media generates additional electrical conductivity pathways along the clay surface that must be corrected (Mavko et al., 2009). The most accepted correction is Waxman–Smits–Juhász model (Juhász, 1981), which accounts for the excess of charges through the charge per unit volume (Q_v), and the increased mobility of ions along the clay surface (B) when in contact with an electrolytic solution (Mavko et al., 2009):

$$S_w = \left(\frac{F R_w}{R_b (1 + B Q_v R_w / S_w)} \right)^{1/n}, \quad (4)$$

with the resistivity formation factor $F = a\phi^{-m}$, and

$$B = \frac{-1.28 + 0.225T - 0.4059 \cdot 10^{-4} T^2}{1 + R_w^{1.23} (0.045T - 0.27)}, \quad (5)$$

for temperature (T) in degrees Celsius, and

$$Q_v = \rho_S CEC (1-\phi)/\phi. \quad (6)$$

In the above expression, ρ_s is mineral clay grain density (~2600 kg m^{-3} for chlorite (Mookherjee and Mainprice, 2014)), and CEC the cation exchange capacity ($CEC_{(chorite)}$ = 0.01 meq g^{-1}; (Thomas, 1976)).. The CEC value of our samples can be calculated from their respective mass fractions (x) of chlorite (i.e., CEC = $x_{chlorite}$ x

388 $CEC_{chlorite}$), as the CEC for the rest of the minerals (Table 1) can be neglected. . With
389 the small clay volume fraction with respect to the pore volume of our samples, the
390 high salinity of the pore water and the low CEC of the chlorite, we anticipate very
391 little contribution of clays to the bulk resistivity in our case, with $Q_{v, S-A}$ = 0.0011 $Q_{v, S-B}$= 0.0015.

393 *2.6. Elastic waves modelling: velocity and attenuation*

394 The porosity for both the shallow sandy sediments we tested, as well as that
395 obtained from the wireline logs, is systematically above the critical porosity assumed
396 for sandstones. Critical porosity (ϕ_c, the largest porosity for which the matrix can
397 support itself without the individual grains being considered a suspension) ranges
398 between 36% - 40% for clean- and up to 45% for clay-rich sandstones (Nur et al.,
399 1998). Then, for the elastic modelling of our clay-rich sand, we require a
400 methodology for calculating the dry properties of samples with porosities above ϕ_c.
401 We not that, despite the porosities of both samples being above the ϕ_c, both samples
402 were self supported and did not behave as suspensions, even at low effective
403 pressure..

404 Dvorkin et al. (1999) model's has succeded in replicating the elastic properties
405 of near-surface offshore sediments with high porosity. It assumes Hertzian contacts
406 (e.g., Mavko et al., 2009) with partial consolidation around large voids leading to the
407 higher porosity count, assumptions which we adopt here. As a workflow, input
408 parameters for ϕ_c and grain contacts (n) are unknown in our case but informed
409 choices consistent with values given in Dvorkin et al. (2001) are ϕ_c =0.36 and grain
410 contacts n=9. However, these should be thought of as tuning parameters rather than
411 inverted values. These values are used together with the knowledge of effective
412 pressure to form Hertz-Mindlin moduli (Mavko et al., 2009), which are then averaged

413 with the grain moduli to produce the predicted dry moduli of the shallow sediment
414 frame. The ambiguity in the grain modulus for a polymineralic rock is compensated
415 by taking the Hill average of the moduli of the individual constituents. We used the
416 average of each mineral bulk (K) and shear (G) moduli (Table 2) and perform a
417 common Hill average (Mavko et al., 2009) to calculate effective grain moduli. This
418 averaging justifies assuming constant mineralogy for simplicity as the average elastic
419 properties do not change much with depth despite the variation in the individual
420 constituents.

421 We model the velocity as a function of depth for the log using Gassmann's
422 model (Gassmann, 1951), whose assumptions for a well connected pore space are
423 satisfied in this case (Dvorkin et al., 1999). The porosity and the effective
424 (hydrostatic – lithostatic) pressure are assumed to be functions of depth whereas the
425 remaining parameters, in particular the mineralogy, are assumed constant. Then, we
426 model the partial saturated states using Gassmann's formula and the effective fluid
427 modulus for different fluid distribution scenarios (uniform q = 1, or patchy saturated
428 matrix $q = K_{CO2}/K_{brine}$, with K being the fluid modulus), by means of the patch
429 parameter q in Papageorgiou et al. (2016).

430 Table 2. Properties and mineralogy used in the modelling of samples A and B (values from
431 Mavko et al. (2009))

	K (GPa)	G (GPa)	density (Kg m^{-3})	Reference
Minerals				
Orthoclase	37.5	15	2620	(Mavko et al., 2009) *(Mookherjee and Mainprice, 2014)
Plagioclase	75	25	2630	
Calcite	70	30	2700	
Dolomite	70	50	2880	
Quartz	37	44	2650	
*Chlorite	155	51	2600	
Mica	62	41	2790	

Dry sample				
S-A	0.27	0.36	1456	Hertz-Mindlin moduli (Mavko et al., 2009)
S-B	0.21	0.26	1196	
Fluids				
CO_2	0.05	10^{-7}	25.6	(Span and Wagner, 1996)
Brine	2.39	10^{-7}	1024	(Batzle and Wang, 1992)

Gas propagation trough the brine saturated sediment can be by capillarity or fracture opening (Boudreau, 2012; Roche et al., 2021), with the latter leading to grains displacement and rearrengement.. The amount of CO_2 injected is larger than the solubility limit of CO_2 in brine for our experimental PT and salinity conditions (Duan et al., 2006), and isolate bubbles may form and migrate in our soft and cohesive samples, particularly in our S-B (muddy sample). Hence, we expect gas bubble resonance effects, which would affect both ultrasonic elastic velocity and attenuation. To consider this effect, we also adapt the effective medium rock physics model by Marín-Moreno et al. (2017), initially developed for gas hydrate bearing sediments (e.g., Sahoo et al., 2018; Sahoo et al., 2019), to account for CO_2 gas effects in partially saturated sediments with no hydrate. This model considers frequency-dependent energy disipication due to wave-induced oscillating gas bubbles in a dilute gas-liquid mixture due to viscous, thermal, and inertial (Biot's) properties based on the approach of Smeulders and Van Dongen (1997). This model complements the fluid distribution modelling described above, by providing further information about the way CO_2 bubbles may propagate across the sample.

For the modelling, we use elastic paramerters shown in Table 2, assuming the experimental conditions of effective pressure (0.1 MPa), the pore pressure of the CO_2 when being injected(1.3 MPa) and temperature (20° C).

3. Experimental results and data analysis

3.1. BCFT Tests

Figure 3 shows the geophysical and hydromechanical results of the brine and CO_2 flow-through tests performed on the POS527-GC06 core samples S-A (~1 mbsf, sandier) and S-B (~2.1 mbsf, muddier). Both tests were actively running for ~4.5 h, resulting in ~28 pore volume (PV) throughputs (~4 PV of brine; ~24 PV of CO_2) each.

The permeability during the brine flow stage (i.e., absolute permeability to brine) of both samples is above 10^{-16} m^2, at seafloor conditions. These values are up to two orders of magnitude lower than those estimated theoretically from grain size distributions (Figure 1). This incongruence might be related to the stress sensitivity of the permeability, which is particularly significant for S-B. This effect can be linked to the generation of favourably oriented microcracks, which preferentially appear in fine-grained materials even for very low changes in effective stress (Bolton et al., 2000). The axial strain record also indicates that S-B is more deformable than S-A, although in general terms both samples show very little deformation (<0.01%) at the experimental conditions. Note the permeability at the end of the brine flow stage is obtained at the most realistic state of stress for 1 and 2.1 mbsf (i.e., S-A and S-B), with $k_{S\text{-}A}$ = 2 x 10^{-15} m^2 and $k_{S\text{-}B}$ = 3 x 10^{-17} m^2.

After initiating the CO_2 injection, the differential pore pressure (ΔP_p) suffers sudden increases in both tests (up to 0.2 and 0.07 MPa for S-A and S-B, respectively), which are later gradually recovered. . Then, following these peaks, the pore pressure up- (P_u) increases with the flow rate in the muddier sample (S-B), but not the ΔP_p; while in the sandier sample (S-A), ΔP_p increases with the flow rate. In turn, the k_{eff} increases gradually in S-A (up to 10^{-13} m^2), and abruptly in S-B (up to

477 10^{-14} m^2), which suggests that the increasing CO_2 flow rate preferentially generated
478 path-flows in the muddier sample. This observation is supported by the little variation
479 in the bulk electrical resistivity for the sample S-B with respect to S-A.
480 P-wave attributes (velocity, V_P, and attenuation, Q_p^{-1}) are generally very good
481 indicators of both the deformation and pore fluid distribution (e.g., Falcon-Suarez et
482 al., 2017). V_P varies with the confining pressure during the brine flow, inversely
483 following the axial strain trends. Then, in both tests, the arrival of the CO_2,
484 corroborated by a resistivity increase, triggers an initial sharp drop in V_P of ~1%.
485 Thereafter, V_P shows a slight gradual decrease until the end of the tests. Contrarily,
486 Q_P^{-1} is very little affected by changes in the state of stress in both samples, but
487 sharply increases by ~60% when free CO_2 is present in the porous medium.

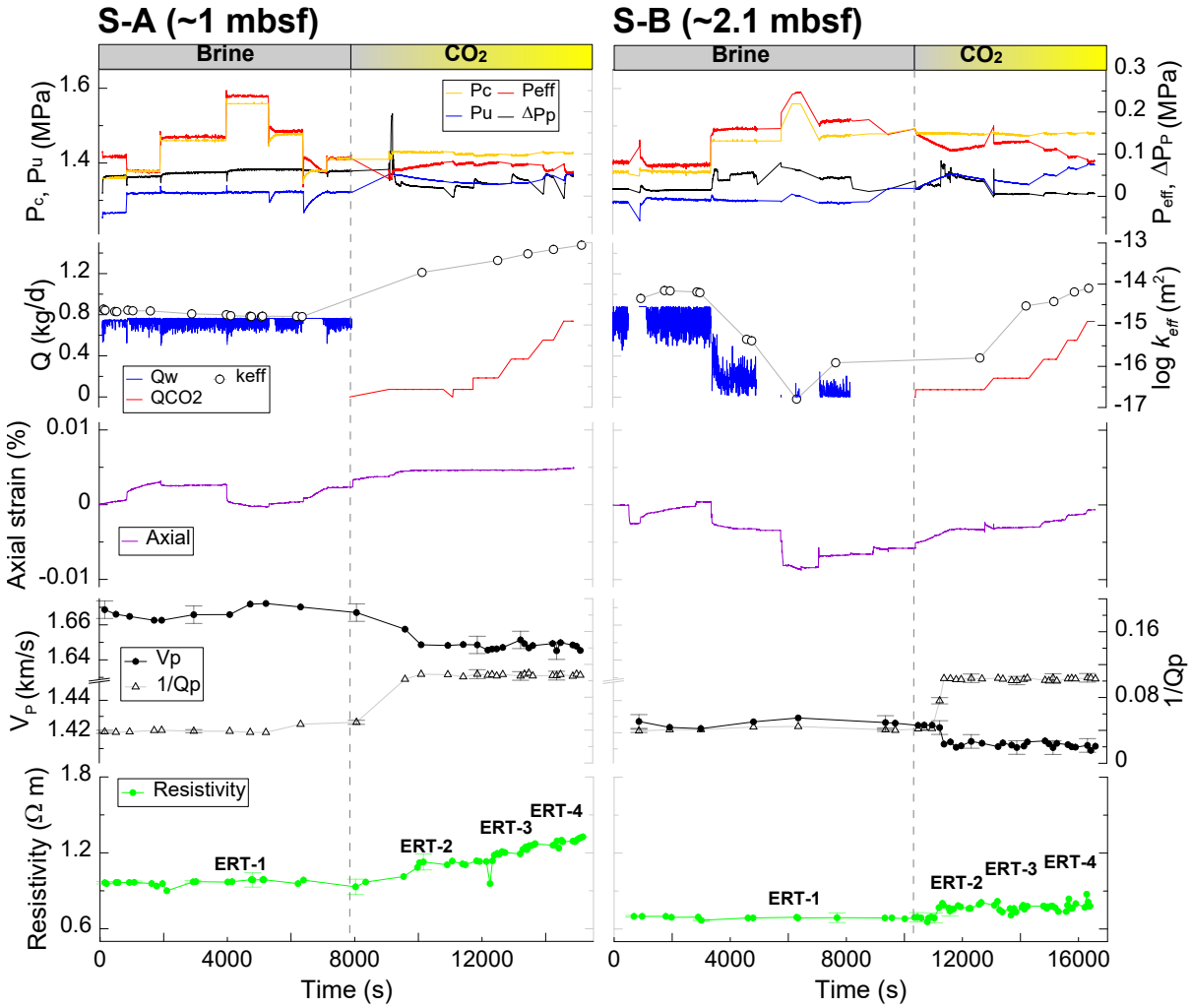

Figure 3. Brine-CO_2 flow-through tests performed on POS527-GC06 core samples S-A (~1 mbsf) and S-B (~2.1 mbsf). P-wave velocities (V_P) and attenuation (Q_P^{-1}), electrical resistivity, axial strains, partial flow rates for CO_2 (Q_{CO2}) and brine (Q_w), confining (P_c), effective (P_{eff}), upstream (P_u) and differential (ΔP_p) pore pressure are plotted together with effective permeability (k_{eff}). The ultrasonic properties were measured at a single frequency of 600 kHz (pulse-echo technique), obtained from Fourier analysis of broad band signals.

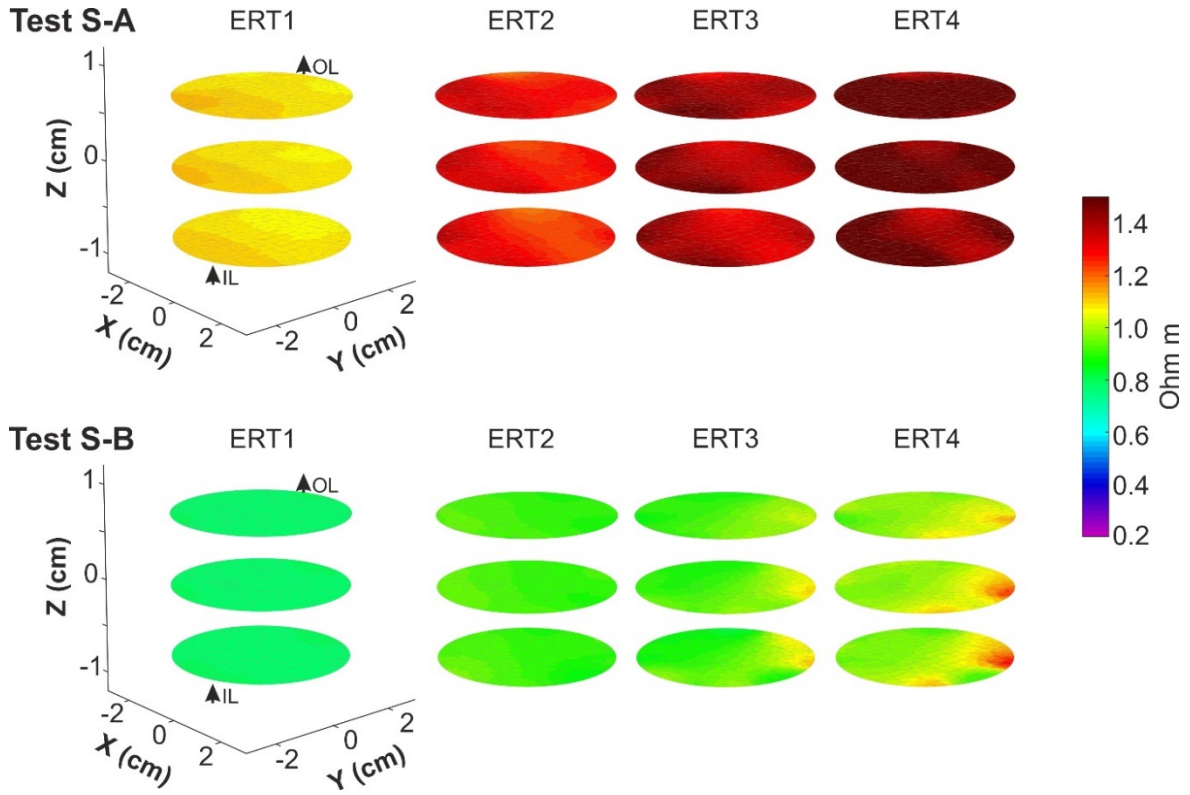

497

498 Figure 4. Electrical resistivity tomography of the two samples at different stages of the tests
499 (ERT1 to 4 in Figure 3), represented as three slices of the samples at -0.75, 0 and 0.75 cm
500 height with respect to the sample centre. The dimensions are only represented in the first
501 (left) tomography image, as well as the flow inlet (IL) and outlet (OL) ports, for clarity.

502 Electrical resistivity is slightly higher in sample S-A. Since both samples were
503 saturated with the same brine, this difference might be associated with the internal
504 grain distribution, heterogeneities and mineral composition (Falcon-Suarez et al.,
505 2020a). ERT images (Figure 4) revel that sample S-B had a more heterogeneous
506 electrical distribution with the increasing CO_2 content, corresponding to the more
507 resistive locations. This observation agrees with previous studies, which suggest that
508 grain size conditions the CO_2 distribution within the sediment, becoming more
509 homogeneous from clay- to sand-rich layers (e.g., Cevatoglu et al., 2015; Roche et
510 al., 2021). The patchy distribution of high electrical resistivity at the lateral of the
511 sample with vertical continuity indicates a preferential channel for CO_2 percolation,

512 with a horizontal section increasing with the flow rate from 5 mm (ERT 3; Q_{CO2} =
513 0.55 kg d^{-1}) to ~10 mm (ERT4; Q_{CO2} = 0.74 kg d^{-1}).

514 *3.2. Estimation of CO_2 saturation*

515 After each test, the final CO_2 saturation ($S_{CO2,f}$) achieved in each sample was
516 preliminary estimated by mass balance (oven-dried at 60 C), resulting in a $S_{CO2,f}$
517 ~0.35 for the sample S-A, but $S_{CO2,f}$ ~0.13 for the sample S-B. However, the best
518 fitting curve to the resistivity data led to a $S_{CO2,f}$ of 0.18 ± 0.05 for S-A and 0.09 ±
519 0.05 for S-B. The adjustment of the empirical parameters *a*, *n*, and *m* (Table 3) in
520 expression (4) was carried out by non-linear least squares from the resistivity data
521 collected during the tests (Figure 3). The CO_2 excess obtained by mass balance in
522 both cases may be linked to brine drainage post-test induced by gas expansion and
523 exolution during the controlled decompression. Despite S-B is a porous medium with
524 higher capillary forces than S-A, it showed a lower CO_2 excess. This contradiction
525 suggests the CO_2 advanced more homogeneously distributed through sample S-A,
526 which agrees with the electrical distribution observations (Figure 4).

527 Table 3. Fitting parameters for the transformation of resistivity into degree of saturation

Sample	Depth (mbsf)	*a*	*m*	*n*
S-A	1.0	1.04	1.93	1.8
		1.02	1.83	2.0
S-B	2.1	1.01	1.78	2.2
		1.05	1.98	1.8
		1.04	1.94	2
		1.03	1.88	2.2

528

529 The resistivity-saturation transformation carries several uncertainties related to
530 the accuracy of our sensors, the effect of the dissolved CO_2, and the potential CO_2-
531 induced porosity changes. Falcon-Suarez et al. (2018) found that the geophysical
532 tools used for this experiment were unable to detect the effect of the dissolved CO_2

533 on both the bulk resistivity and P-wave velocity under similar T-salinity conditions but
534 higher pressure (i.e., up to three times higher dissolved CO_2, according to Duan et
535 al. (2006)). This is in agreement with Börner et al. (2013), who found that brine
536 salinities as high as the one used here mask effect of dissolved CO_2. In other words,
537 the dissolved CO_2 is below our experimental error, and therefore neglected in our
538 conversion.

539 The porosity increase associated with the partial dissolution of the carbonate
540 fraction (originally porosity) is an additional source of uncertainty. Reactive transport
541 models suggest these sediments have very low reactivity to CO_2 (Marín-Moreno et
542 al., 2019). According to the dissolution rates observed by Lichtschlag et al. (2021),
543 for this core sample under laboratory conditions (i.e. 20°C and 1 bar), the short time
544 exposure of our samples to CO_2 (~2 h) led to variations of the carbonate content
545 from before to after the tests lying within the uncertainty of the measurement (± 0.3
546 wt%) in both cases. Therefore, in our resistivity-saturation model, we assume no
547 porosity variations due to dissolution/precipitation processes and no associated
548 changes in brine resistivity.

549 Figure 5a shows the resistivity-saturation models for S-A and S-B, using the
550 Archie's law modified to account for the effect of clay on the bulk resistivity, while the
551 fitting parameters of the resistivity-saturation model are shown in Table 3.

552 Then, assuming the brine saturation condition (i.e., S_w = 1), we apply the two
553 models to the core log resistivity data (Figure 5b) to estimate the porosity from
554 expressions (4). For comparison, in Figure 5b we display two additional models
555 considering m = 1.5 and m = 1.9, with a =1 in both cases, to frame the accepted
556 cementation range for high porosity unconsolidated granular sediments (Jackson et
557 al., 1978; Mavko et al., 2009)). As a reference, the former case (i.e., m = 1.5)

coincides with that adopted by Gehrmann et al. (2021) to estimate the porosity of the Witch Ground Formation from MSCL resistivity data, while the latter case is closer to that used by Schwalenberg et al. (2020) for the Danube deep-sea fan, Black Sea. The Archie's model for S-A matches better the measured (MSCL) data at lower porosities (i.e., sandier levels), while the S-B one works better for higher porosities (i.e., muddier levels). The upmost part of the sediment column is poorly fitted by high cementation exponents, likely related to an increase of the grain sphericity with the grain size increase upwards (see Figure 1).

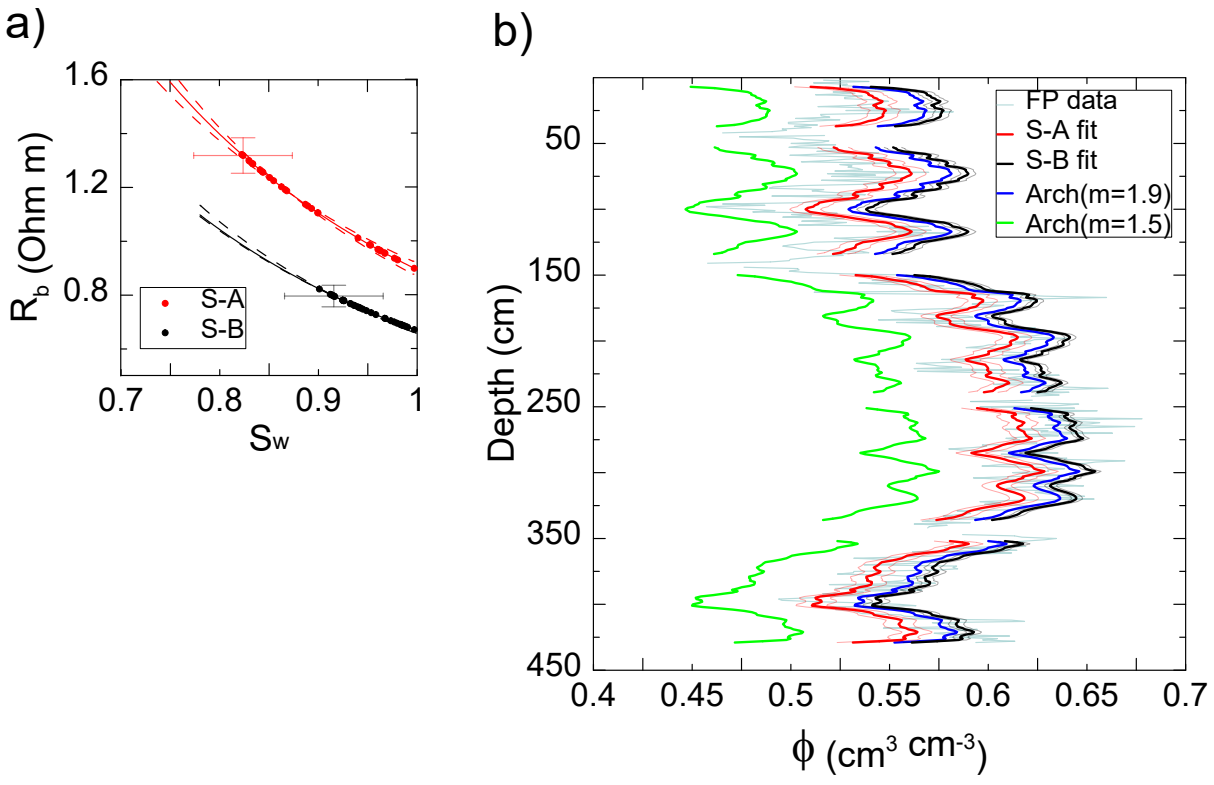

Figure 5. (a) Resistivity into degree of brine saturation applying classic Archie's first and second law accounting for the shale correction (see text for details) for samples S-A and S-B, with dashed lines representing the boundaries associated with ±10% variation in saturation parameter *n*. (b) Porosity variations with depth calculated from the MSCL resistivity data using the Archie's fittings for S-A and S-B, with thin lines representing the boundaries associated with ±10% variation in saturation parameter *n* (see Table 3), and two additional fittings using classic Archie model, adopting m = 1.5 and m = 1.9, respectively, together with the formation porosity data, FP, from MSCL for reference.

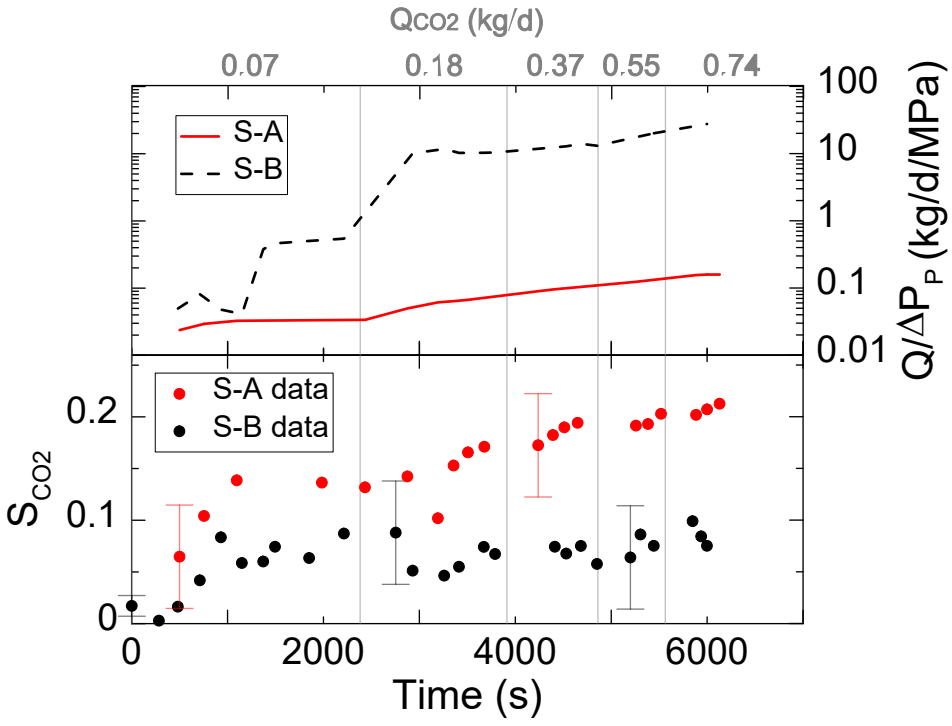

Figure 6. Evolution of the degree of CO_2 saturation (S_{CO2}) and the outlet flow versus differential pore pressure gradient ($Q/\Delta P_p$).. S_{CO2} uncertainties derived from the most conservative error in resistivity (see text).

The CO_2 saturation (S_{CO2}) increases with the increasing CO_2 flowrate during laboratory tests (Figure 6). For sample S-A, the S_{CO2} increases gradually with time,

585 while S-B shows a prompt increase during the first CO_2 injection stage and remain
586 constant afterwards. The $Q/\Delta P_p$ gradient is an indicator of how easy the CO_2 flows
587 through the sample for a given SCO_2 value. This gradient increases gradually with
588 SCO_2, as expected, for S-A; for S-B, the gradient sharply increases, regardless of
589 the SCO_2 that remains constant, which indicates the gradient is still below the
590 threshold value for the flow pathway generated during the first CO_2 flowrate stage.
591 This observation supports the generation of preferential paths for CO_2 flow in sample
592 S-B interpreted from the ERT data.

593 *3.3. Acoustic P-waves*

594 Ultrasonic P-wave velocities (V_P) and attenuations (Q_P^{-1}) vary with the CO_2
595 content, particularly for $S_{CO2} > 0.05$ (Figure 7). V_P decreases by 1.1% and 0.8% for
596 S-A and S-B, respectively, while Q_P^{-1} increases by 58% and 63% for S-A and S-B,
597 respectively. V_P variations are very low compared to previous experimental data
598 obtained on reservoir rocks, which report drops above 7% at the arrival of the free-
599 phase CO_2, progressively increasing with S_{CO2} up to above 25% (e.g., Falcon-
600 Suarez et al., 2018; Kim et al., 2013; Kitamura et al., 2014). Q_P^{-1} shows similar
601 values than to previously reported data (e.g., Alemu et al., 2013; Falcon-Suarez et
602 al., 2018), and clearly indicates the arrival of the CO_2 in the pore space; but the
603 quantification of the saturation using Q_P^{-1} may lead to misleading interpretation if
604 fracturing and fluid substitution occur simultaneously (Falcon-Suarez et al., 2020b).
605

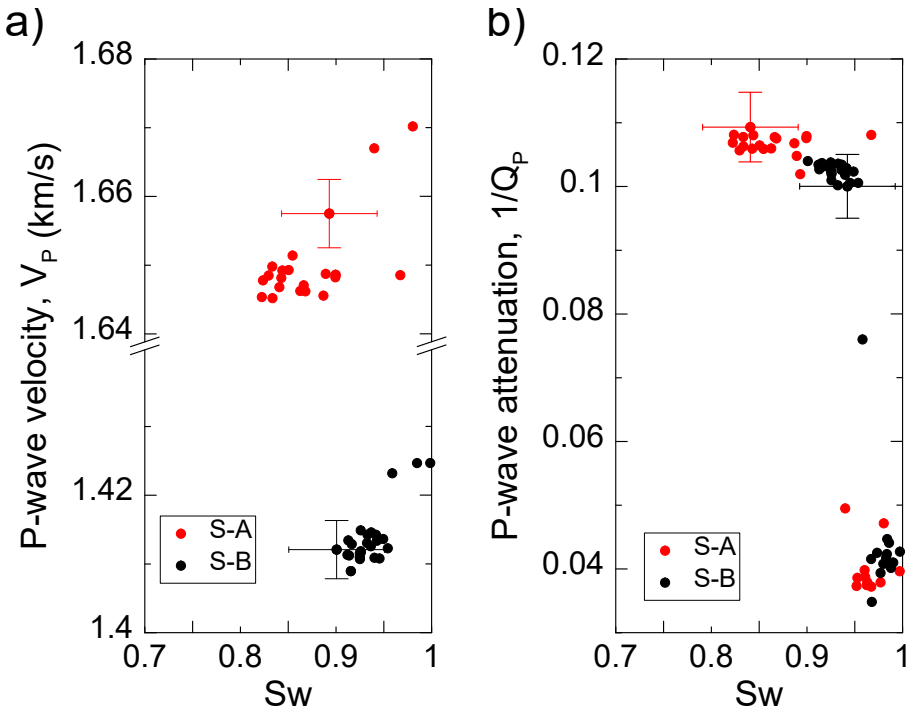

606

607 Figure 7. P-wave (a) velocity V_P and (b) attenuation Q_P^{-1} versus degree of brine saturation
608 for the samples S-A and S-B. Only one cross-error bar per sample is displayed for clarity.

609 Dvorkin et al. (1999)'s model predicts reasonably well the V_P from the MSCL
610 analysis on the gravity core POS527-GC06 below 1.5 mbsf, when considering the S-
611 B mineralogy for the fitting (Figure 8). If the model is based on the S-A mineralogy,
612 the fitting offers good results within the range 1-1.5 mbsf, only. Above 1.5 mbsf, the
613 overestimation of the MSCL data indicates a mineralogical change disregarded by
614 the model, perhaps related to an increment of chlorite. The elastic moduli of chlorite
615 are up to one order of magnitude higher than other clay minerals (e.g., Mavko et al.,
616 2009), and exhibits the greatest moduli among the minerals present in our samples
617 (Table 2). Also chlorite present significant anisotropy, with greater elastic moduli in
618 the direction perpendicular to the basal plane (Mookherjee and Mainprice, 2014),
619 coinciding with the lamination in our case. Note that the MSCL measures V_P
620 perpendicular to the core axis (Geotek, 2016), which in this case is perpendicular to
621 the bedding and therefore aligned with the lower component of the chloride

anisotropy. As grain size and sphericity varies upwards, we expect chlorite grains to be more randomly oriented and thus increasing the mean elastic moduli of the minerals. We also predict V_S from this model (Figure 8), although no log data exist to compare it to. However, we anticipate that the shear modulus, therefore the shear velocity, is to some extent overestimated, as it is commonly the case of with assuming Hertzian contacts for high porosity formations (Mavko et al., 2009).

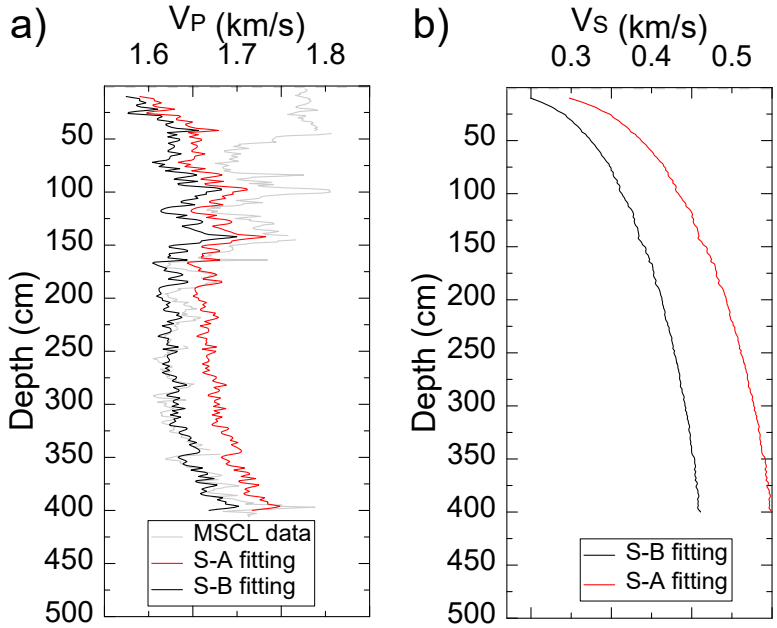

Figure 8. (a) P-wave velocity from MSCL and estimates from the Dvorkin et al. (1999)'s model, and (b) S-wave velocities estimates with depth.

Discrepancies in the absolute values between logging and ultrasonic velocities in our case are related to two opposing effects: the frequency of the measurements and the direction of wave propagation with respect to sediment foliation. V_P increases with frequency for a given material (Batzle et al., 2006); but, for a given frequency V_P decreases with the wave propagation angle with respect to the lamination plane (e.g., Best et al., 2007; Falcon-Suarez et al., 2020a). Our samples present lamination only distinguished by colour gradation, with a bedding thickness in the order of the grain size (i.e., <0.063 mm). From our V_P values and the

639 frequency of measurement (f = 600 kHz), we obtain a wavelength ($\lambda = V_P / f$) of ~2.5
640 mm. With the wavelength above the bedding thickness, the medium is seen as
641 homogeneous. However, Best et al. (2007) found that thin layering on a scale of less
642 than 0.1 of the wavelength is the dominant cause of velocity and attenuation
643 anisotropy in siltstones and sandstones.
644 The MSCL velocity (at 230 kHz) should be lower than our ultrasonic one (at 600
645 kHz), but the former is measured across the core section and therefore parallel to
646 the bedding plane (i.e., fastest V_P component). Conversely, in the flow-through tests
647 we measure the ultrasonic velocity perpendicular to the layering (i.e., slowest V_P
648 component). Comparing the change in velocity with frequency reported by Batzle et
649 al. (2006) and the deviation due to the wave-to-layer orientation reported by Best et
650 al. (2007) or Falcon-Suarez et al. (2020a), we observe the orientation affects more
651 the velocity for the fully saturation case. The orientation impact increases with the
652 layering-induced anisotropy, ultimately conditioned by the microstructure (Falcon-
653 Suarez et al., 2020a), which is presumably more pronounced for sample S-B with a
654 higher clay content (Figure 1). This would explain the higher discrepancy between
655 the MSCL (Figure 8) and ultrasonic measurements for S-B fully (brine) saturated
656 (Figure 9a).
657

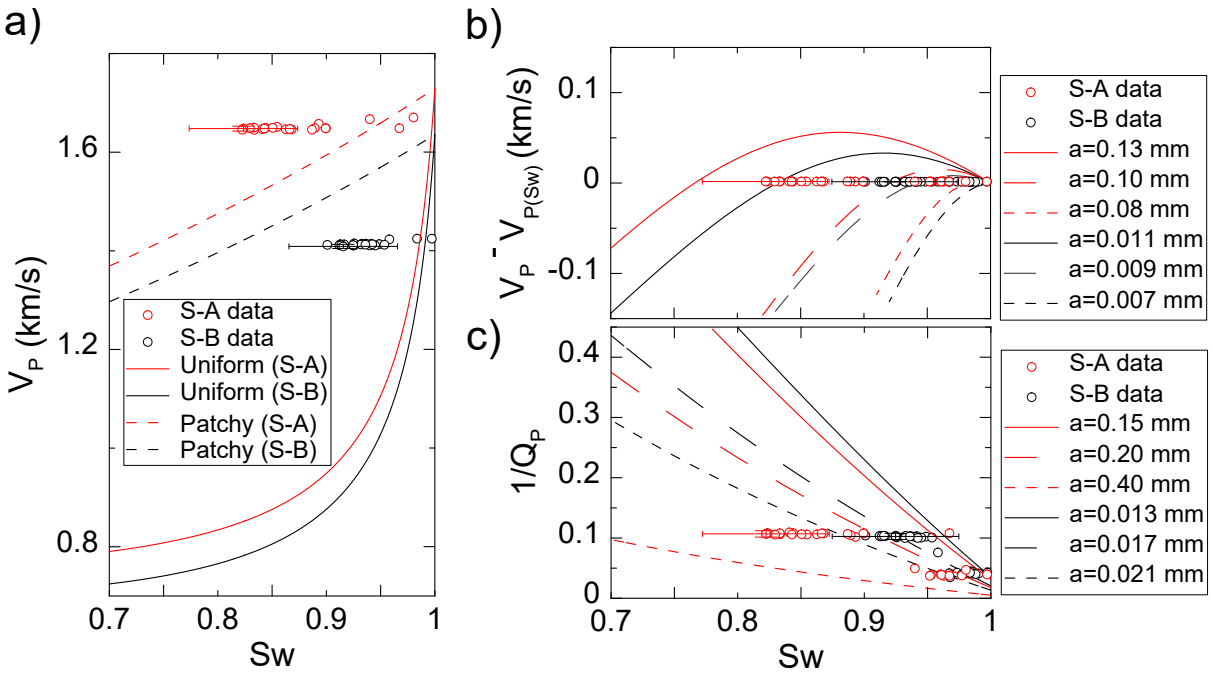

Figure 9. (a) P-wave velocity V_P versus degree of saturation S_w estimates from combining the models of Dvorkin et al. (1999) and Papageorgiou et al. (2016) for the patchy and uniform pore fluid distribution cases. The resonance model of Marín-Moreno et al. (2017) expressing CO_2 bubble size in terms of (b) the P-wave velocity difference with respect to that under fully brine saturation conditions (V_P - $V_{P(Sw)}$) and (c) the P-wave attenuation (Q_P^{-1}) for different bubble radius *a*.

The measured V_P value at full water saturation for sample S-B lies just below the V_P corresponding to the lower Hashin-Shtrikman bound (Figure 9a), calculated in 1.48 km s^{-1} for S-B using the methodology in Berryman (1995), which indicates that the moduli for this sample using the mineralogy of Table 2 are overstimated. The V_P measurement for sample S-A, however, is close to the value predicted by the Dvorkin et al. (1999)'s model when the matrix is fully water saturated (~1.69 km s^{-1}), indicating a higher degree of consolidation but still a poor dependence on CO_2. In this regard, inasmuch as CO_2 induced pathways can be inferred from the heterogeneous resistivity distribution (Figure 4), the elastic modelling considering patchy fluid distribution is more appropriate to explain the results (Figure 9a).

675 However, our modelling approach for partial saturation is unable to explain the
676 experimental data. These discrepancies might be related to the fact that our model
677 considers homogeneous samples, while our results suggest the decrease in effective
678 pressure during CO_2 injection led to generate some degree of fracturing.
679 The analysis of the gas bubble resonance effect (Figure 9b,c) shows that,
680 although for both tests the bubble size increases with the CO_2 saturation, the
681 maximum size that explains the data is more than 10 and 100 times smaller than the
682 sample lengths of S-A and S-B, respectively. This observation suggests the
683 preferential path flows consisted of interconnected sub-vertical narrow fractures, with
684 apertures lower than the maximum bubble size, where the CO_2 propagation occurs
685 as a discontinuous gas phase. This propagation would be invisible to the ERT
686 images and therefore it has to be taken hypothetically. The fact that when increasing
687 the saturation a larger radius matches the data better, may imply buble aggregation
688 with the increasing S_{CO2} or CO_2 flowrate. Our results are in similar range as those
689 reported by Choi et al. (2011) for similar sediments and environmental and
690 conditions.

691 **4. Discussion**

692 We found that near-seafloor sediments affected by CO_2 venting can retain
693 CO_2, with greater efficiency in coarser-grained (e.g., sample S-A) layers, despite
694 their lower porosity and larger permeability. Finer-grained (sample S-B like) layers
695 are more sensitive to changes in the effective stress, and prone to develop
696 preferential pathways (fracturing) under similar venting conditions, as previously
697 reported (Deusner, 2016; Robinson et al., 2021). This observation supports the idea
698 that the microstructure of shallow offshore sediment conditions the final stage of the

699 CO_2 migration from deep geological reservoirs before reaching the water column
700 (Cevatoglu et al., 2015; Roche et al., 2021).
701 Coarse-grained sediments, with low capillary forces, allows percolation
702 (capillary invasion) and CO_2 partially saturates the sediment; in fine-grained
703 cohesive sediments, the gas propagation causes sediment fracturing by displacing
704 the grains (e.g., Boudreau, 2012). Then, sample S-A was preferentially subjected to
705 capillary invasion as deduced from the increasing CO_2 saturation trend with the
706 injection rate (Figure 6), while the invariable trend for S-B suggests a fracture-
707 dominated regime since very early stages of the test. In this regard, the higher
708 stress-sensitivity of the permeability observed in S-B could be attribute to the
709 presence of cracks existing pre-CO_2 injection, which facilitated the development of
710 CO_2 migration pathways by fracture reopening. Robinson et al. (2021) show cores
711 from the same North Sea area, with similar sediment properties, which contained
712 internal structures that might be acting as precursor discontinuities for fracturing.
713 Induced fracturing hypothesis is also supporting the higher increase of effective
714 permeability for S-B than for S-A, by three and two orders of magnitude relative to
715 the fully saturated background permeability, respectively.
716 The electrical resistivity tomography confirmed the heterogeneous CO_2
717 distribution in sample S-B, although the resolution of the tomography is unable to
718 detect minor fracturing. The calculated CO_2 saturation values, ranging from S_{CO2} 0.1
719 ± 0.05 (S-B) to ~0.18 ± 0.05 (S-A), agree reasonably well with the estimate of S_{CO2} =
720 0.1 ± 0.03 obtained from the data collected in the field during the STEMM-CCS
721 release experiment (Roche et al., 2021). Roche et al.'s estimate is based on the
722 volumetric positive deformation observed in the seafloor during the release
723 experiment, accounting for the first three metres below the seafloor that combine

724 coarse- and fine-grained layers. Although our results indicate very low sample
725 deformation in both tests, the difference with respect to the values observed in the
726 field is likely related to the higher hydraulic energy used in the latter case (from 8 x
727 10^{12} m^3 km^2 y^{-1} at the injecting point for the first CO_2 injection step (Flohr et al.,
728 2021)). That hydraulic energy was four orders of magnitude higher than the flow
729 conditions of our lab tests (from 5 x 10^8 m^3 km^2 y^{-1}) .
730 The potential CO_2-induced crack development in S-A and S-B would be also
731 affecting the interpretation of our ultrasonic measurements, due to fracture features
732 and orientation. Assuming the case of stable fracture propagation in our tests, the
733 fracture length (c) varies within the range 2.5 - 3.0 mm and the elongation is
734 preferentially vertical (Roche et al., 2021). According to our wavelength (λ ~2.5 mm),
735 with $c / \lambda \geq 1$ the medium is seeing as heterogeneous, with the cracks acting as
736 energy scattering fronts (Falcon-Suarez et al., 2020b). Furthermore, when fractures
737 are aligned vertically (i.e., in the direction of the wave propagation), the V_P drop from
738 fully to partially saturated medium (for $S_w > 0.7$) is minimum (Amalokwu et al., 2015;
739 Amalokwu et al., 2017), and the same effect was recently observed in the oblique
740 fractures case (Falcon-Suarez et al., 2020b).
741 Previous studies show that the gas phase tends to preferentially occupy larger
742 pore cavities (e.g., Muñoz-Ibáñez et al., 2019), which for the case of vertical
743 fractures means that wave propagation between cracks occurs at near fully
744 saturation conditions. This CO_2-induced crack size-elongation combined effect would
745 explain the low velocity and high attenuation changes with the CO_2 arrival. Our
746 ultrasonic data therefore evidence the potential of the P-wave attenuation to infer the
747 presence of CO_2, but at the same time the low sensitivity of this signature for S_{CO2}
748 quantification (i.e., very little variation afterwards). Interestingly, our results are in

749 agreement with the attenuation trend observed in the seismic dataset collected
750 during the STEMM-CCS CO_2 release experiment (Roche et al., 2021).
751 The small change of V_P in CO_2-brine partially saturated systems containing
752 vertical fractures can be seen from wave frequencies above seismic (f > 200 Hz;
753 (Solazzi et al., 2020)). This observation might affect the identification and
754 interpretation of seal bypass systems with dimensions below seismic resolution,
755 which can even be more effective bypass structures than their larger scale seismic
756 chimneys analogues (Cartwright et al., 2007). In this regard, Waage et al. (2021)
757 found that detectable geophysical signatures of partial CO_2 saturation structures
758 using high-resolution P-Cable 4D seismic method (with f = 500 Hz), highly depends
759 on the pore fluid distribution, with a low detection limit of S_{CO2} ~3% for uniform
760 distribution but up to ~27% if patchy. This S_{CO2}-patchy value is in agreement with our
761 experimental observations, Amalokwu et al. (2017) and Falcon-Suarez et al. (2020b)
762 for sandstones with oriented fractures at ultrasonic frequencies, and can be
763 expected above 200 Hz according to the modelling results reported by Solazzi et al.
764 (2020) if just considering the hypothesis of CO_2-induced sub-vertical fractures.
765 Our core scale data contribute to the multi-scale and multi-disciplinary
766 characterization required for the understanding of the upper part of fluid scape
767 structures (Robinson et al., 2021), by generating geophysical data related to the
768 hydromechanical response of shallow coarser and finer grained sediments affected
769 by free CO_2 gas migration, in a controlled manner. New rock physics modelling
770 approaches combining dispersion due to gas-induced fracturing near the
771 suspension/cohesion limit might help improve the quantification of gas and fluid
772 phases of seafloor sediments, and the interpretation of pockmarks and fluid scape
773 structures underneath.

5. Summary and conclusions

We have studied the response of shallow sub-seafloor, poorly consolidated sediments to CO_2 gas migration. We have conducted brine-CO_2 flow-through tests with geophysical, hydraulic and mechanical monitoring in the laboratory, using two North Sea seabed sediment samples with different granular distribution. Our data can be used to calibrate geophysical datasets collected during STEMM-CCS and CHIMNEY projects, including the CO_2 release experiment of May 2019 (Flohr et al., 2021), and may help improve the general interpretation of shallow sub-seafloor gas (mainly CO_2 and methane) distribution and migration patterns.

With respect to the geophysical tools we used for CO_2 distribution monitoring, we found that the transformation of resistivity into degree of saturation based on Archie's relationship improves when considering the grain size distribution of the samples. Our ultrasonic P-wave attributes detected the presence CO_2, with the attenuation factor showing clearer signatures; but both fail in providing accurate estimates of the CO_2 saturation.

We found that the permeability of the sediments tested varies from ~10^{-15} m^2 to ~10^{-17} m^2, decreasing with the grain size. When subjected to CO_2 venting at near seabed conditions, these sediments may develop some degree of fracturing, particularly for the finer-grained sediments as evidenced by a sharp increase of the effective CO_2 permeability.

Acknowledgments

The experiment was conducted at the NOC Rock Physics Laboratory in Southampton. We also thank the British Ocean Sediment Core Research Facility

(BOSCORF) for their contribution to this work, and Richard Pearce regarding the XRD analysis.

Funding

We have received funding from the UK's Natural Environment Research Council grants NE/R013535/1 GASRIP and NE/N016041/1 CHIMNEY, and the European Union's Horizon 2020 research and innovation programme grant No. 654462 STEMM-CCS.

References

Achterberg, E.P., Esposito, M., 2018. RV POSEIDON Fahrtbericht / Cruise Report POS527 - Baseline Study for the Environmental Monitoring of Subseafloor CO_2 Storage Operations, in: Report, G. (Ed.), N. Ser. 045, GEOMAR Helmholtz-Zentrum für Ozeanforschung Kiel, Kiel, Germany, p. 90. https://doi.org/10.3289/geomar_rep_ns_45_2018.

Adler, A., Lionheart, W.R.B., 2006. Uses and abuses of EIDORS: an extensible software base for EIT. Physiological Measurement 27, S25-S42. 10.1088/0967-3334/27/5/s03.

Alemu, B.L., Aker, E., Soldal, M., Johnsen, Ø., Aagaard, P., 2013. Effect of sub-core scale heterogeneities on acoustic and electrical properties of a reservoir rock: a CO_2 flooding experiment of brine saturated sandstone in a computed tomography scanner. Geophysical Prospecting 61, 235-250. https://doi.org/10.1111/j.1365-2478.2012.01061.x.

Amalokwu, K., Chapman, M., Best, A.I., Minshull, T.A., Li, X.-Y., 2015. Water saturation effects on P-wave anisotropy in synthetic sandstone with aligned

fractures. Geophysical Journal International 202, 1088-1095. https://doi.org/10.1093/gji/ggv192.

Amalokwu, K., Papageorgiou, G., Chapman, M., Best, A.I., 2017. Modelling ultrasonic laboratory measurements of the saturation dependence of elastic modulus: New insights and implications for wave propagation mechanisms. International Journal of Greenhouse Gas Control 59, 148-159. http://dx.doi.org/10.1016/j.ijggc.2017.02.009.

Archie, G.E., 1942. The electrical resistivity log as an aid in determining some reservoir characteristics. Society of Petroleum Engineers. https://doi.org/10.2118/942054-G.

Batzle, M.L., Han, D.-H., Hofmann, R., 2006. Fluid mobility and frequency-dependent seismic velocity-Direct measurements. Geophysics 71, N1-N9. https://doi.org/10.1190/1.2159053.

Batzle, M.L., Wang, Z., 1992. Seismic properties of pore fluids. Geophysics 57, 1396-1408. https://doi.org/10.1190/1.1443207.

Berryman, J.G., 1995. Mixture theories for rock properties. Rock Physics & Phase Relations, 205-228. https://doi.org/10.1029/RF003p0205.

Best, A.I., 1992. The prediction of the reservoir properties of sedimentary rocks from seismic measurements. University of Reading, p. 393.

Best, A.I., Sothcott, J., McCann, C., 2007. A laboratory study of seismic velocity and attenuation anisotropy in near-surface sedimentary rocks. Geophysical Prospecting 55, 609-625. https://doi.org/10.1111/j.1365-2478.2007.00642.x.

Blackford, J., Bull, J.M., Cevatoglu, M., Connelly, D., Hauton, C., James, R.H., Lichtschlag, A., Stahl, H., Widdicombe, S., Wright, I.C., 2015. Marine baseline and monitoring strategies for carbon dioxide capture and storage (CCS). International

Journal of Greenhouse Gas Control 38, 221-229. https://doi.org/10.1016/j.ijggc.2014.10.004.

Blott, S.J., Pye, K., 2001. GRADISTAT: a grain size distribution and statistics package for the analysis of unconsolidated sediments. Earth Surface Processes and Landforms 26, 1237-1248. https://doi.org/10.1002/esp.261.

Blouin, A., Sultan, N., Callot, J.-P., Imbert, P., 2019. Sediment damage caused by gas exsolution: A key mechanism for mud volcano formation. Engineering Geology 263, 105313. https://doi.org/10.1016/j.enggeo.2019.105313.

Bolton, A.J., Maltman, A.J., Fisher, Q., 2000. Anisotropic permeability and bimodal pore-size distributions of fine-grained marine sediments. Marine and Petroleum Geology 17, 657-672. http://dx.doi.org/10.1016/S0264-8172(00)00019-2.

Börner, J.H., Herdegen, V., Repke, J.-U., Spitzer, K., 2013. The impact of CO_2 on the electrical properties of water bearing porous media – laboratory experiments with respect to carbon capture and storage. Geophysical Prospecting 61, 446-460. 10.1111/j.1365-2478.2012.01129.x.

Böttner, C., Haeckel, M., Schmidt, M., Berndt, C., Vielstädte, L., Kutsch, J.A., Karstens, J., Weiß, T., 2020. Greenhouse gas emissions from marine decommissioned hydrocarbon wells: leakage detection, monitoring and mitigation strategies. International Journal of Greenhouse Gas Control 100, 103119. https://doi.org/10.1016/j.ijggc.2020.103119.

Boudreau, B.P., 2012. The physics of bubbles in surficial, soft, cohesive sediments. Marine and Petroleum Geology 38, 1-18. https://doi.org/10.1016/j.marpetgeo.2012.07.002.

Bull, J., Berndt, C., Minshull, T., Henstock, T., Bayrakci, G., Gehrmann, R., Provenzano, G., Bottner, C., Schramm, B., Callow, B., Chapman, M., Birinci, H., Yilo,

870 N., Dewar, M., Chen, B., Saleem, U., Marin-Moreno, H., Lichtschlag, A., Falcon-
871 Suarez, I., Roche, B., James, R.H., Connelly, D.P., Matter, J., Elger, J., Karstens, J.,
872 Best, A.I., 2018. Constraining Leakage Pathways Through the Overburden Above
873 Sub-Seafloor CO_2 Storage Reservoirs, 14th Greenhouse Gas Control Technologies
874 Conference (GHGT-14), Melbourne. https://ssrn.com/abstract=3365826.
875 Burnside, N.M., Naylor, M., 2014. Review and implications of relative
876 permeability of CO_2/brine systems and residual trapping of CO_2. International
877 Journal of Greenhouse Gas Control 23, 1-11.
878 http://doi.org/10.1016/j.ijggc.2014.01.013.
879 Cartwright, J., Huuse, M., Aplin, A., 2007. Seal bypass systems. AAPG Bulletin
880 91, 1141-1166. https://doi.org/10.1306/04090705181.
881 Cevatoglu, M., Bull, J.M., Vardy, M.E., Gernon, T.M., Wright, I.C., Long, D.,
882 2015. Gas migration pathways, controlling mechanisms and changes in sediment
883 acoustic properties observed in a controlled sub-seabed CO_2 release experiment.
884 International Journal of Greenhouse Gas Control 38, 26-43.
885 https://doi.org/10.1016/j.ijggc.2015.03.005.
886 Chadwick, R.A., Williams, G.A., Falcon-Suarez, I., 2019. Forensic mapping of
887 seismic velocity heterogeneity in a CO_2 layer at the Sleipner CO_2 storage operation,
888 North Sea, using time-lapse seismics. International Journal of Greenhouse Gas
889 Control 90, 102793. https://doi.org/10.1016/j.ijggc.2019.102793.
890 Choi, J.-H., Seol, Y., Boswell, R., Juanes, R., 2011. X-ray computed-
891 tomography imaging of gas migration in water-saturated sediments: From capillary
892 invasion to conduit opening. Geophysical Research Letters 38.
893 https://doi.org/10.1029/2011GL048513.

894 Dean, M., Blackford, J., Connelly, D., Hines, R., 2020. Insights and guidance
895 for offshore CO_2 storage monitoring based on the QICS, ETI MMV, and STEMM-
896 CCS projects. International Journal of Greenhouse Gas Control 100, 103120.
897 https://doi.org/10.1016/j.ijggc.2020.103120.
898 Deusner, C., Gupta, S., Kossel, E., Freise, M., Anbergen, H., Wille, T., Bigalke,
899 N., Haeckel, M. , 2016. The role of high-pressure flow-through experiments for
900 evaluating the mechanical behaviour of gas hydrate-bearing soils, in: F. Wuttke,
901 S.B., & M. Sanchez (Ed.), Energy Geotechnics. CRC Press.
902 Duan, Z., Sun, R., Zhu, C., Chou, I.M., 2006. An improved model for the
903 calculation of CO_2 solubility in aqueous solutions containing Na^+, K^+, Ca^{2+}, Mg^{2+}, Cl^-,
904 and SO_4^{2-}. Marine Chemistry 98, 131-139.
905 https://doi.org/10.1016/j.marchem.2005.09.001.
906 Dullien, F.A.L., 1992. Porous Media: Fluid Transport and Pore Structure, 2nd
907 Edition ed. Academic Press Inc., San Diego.
908 Dvorkin, J., Nur, A., Huffman, A.R., Bowers, G.L., 2001. Critical-Porosity
909 Models, Pressure Regimes in Sedimentary Basins and Their Prediction. American
910 Association of Petroleum Geologists, p. 0.
911 Dvorkin, J., Prasad, M., Sakai, A., Lavoie, D., 1999. Elasticity of marine
912 sediments: Rock physics modeling. Geophysical Research Letters 26, 1781-1784.
913 https://doi.org/10.1029/1999GL900332.
914 EU CCS Directive, o.G.S.o.C.D., 2009. DIRECTIVE 2009/31/EC OF THE
915 EUROPEAN PARLIAMENT AND OF THE COUNCIL, Official Journal of the
916 European Union p. L 140/114 EN. https://eur-
917 lex.europa.eu/LexUriServ/LexUriServ.do?uri=OJ:L:2009:140:0114:0135:EN:PDF.

Falcon-Suarez, I., Marín-Moreno, H., Browning, F., Lichtschlag, A., Robert, K., North, L.J., Best, A.I., 2017. Experimental assessment of pore fluid distribution and geomechanical changes in saline sandstone reservoirs during and after CO_2 injection. International Journal of Greenhouse Gas Control 63, 356-369. https://doi.org/10.1016/j.ijggc.2017.06.019.

Falcon-Suarez, I., Papageorgiou, G., Chadwick, A., North, L., Best, A., Chapman, M., 2018. CO_2-brine flow-through on an Utsira Sand core sample: Experimental and modelling. Implications for the Sleipner storage field. International Journal of Greenhouse Gas Control 68, 236-246. https://doi.org/10.1016/j.ijggc.2017.11.019.

Falcon-Suarez, I.H., North, L., Callow, B., Bayrakci, G., Bull, J., Best, A., 2020a. Experimental assessment of the stress-sensitivity of combined elastic and electrical anisotropy in shallow reservoir sandstones. Geophysics 85, MR271. https://doi.org/10.1190/geo2019-0612.1.

Falcon-Suarez, I.H., Papageorgiou, G., Jin, Z., Muñoz-Ibáñez, A., Chapman, M., Best, A.I., 2020b. CO_2-brine substitution effects on ultrasonic wave propagation through sandstone with oblique fractures. Geophysical Research Letters 47, e2020GL088439. https://doi.org/10.1029/2020GL088439.

Flohr, A., Schaap, A., Achterberg, E.P., Alendal, G., Arundell, M., Berndt, C., Blackford, J., Böttner, C., Borisov, S.M., Brown, R., Bull, J.M., Carter, L., Chen, B., Dale, A.W., de Beer, D., Dean, M., Deusner, C., Dewar, M., Durden, J.M., Elsen, S., Esposito, M., Faggetter, M., Fischer, J.P., Gana, A., Gros, J., Haeckel, M., Hanz, R., Holtappels, M., Hosking, B., Huvenne, V.A.I., James, R.H., Koopmans, D., Kossel, E., Leighton, T.G., Li, J., Lichtschlag, A., Linke, P., Loucaides, S., Martínez-Cabanas, M., Matter, J.M., Mesher, T., Monk, S., Mowlem, M., Oleynik, A.,

943 Papadimitriou, S., Paxton, D., Pearce, C.R., Peel, K., Roche, B., Ruhl, H.A., Saleem,
944 U., Sands, C., Saw, K., Schmidt, M., Sommer, S., Strong, J.A., Triest, J., Ungerböck,
945 B., Walk, J., White, P., Widdicombe, S., Wilson, R.E., Wright, H., Wyatt, J., Connelly,
946 D., 2021. Towards improved monitoring of offshore carbon storage: A real-world field
947 experiment detecting a controlled sub-seafloor CO2 release. International Journal of
948 Greenhouse Gas Control 106, 103237. https://doi.org/10.1016/j.ijggc.2020.103237.
949 Gassmann, F., 1951. Elastic waves through a packing of spheres. Geophysics
950 16, 673-685. https://doi.org/10.1190/1.1437718.
951 Gehrmann, R.A.S., Provenzano, G., Bottner, C., Marin-Moreno, H., Bayrakci,
952 G., Tan, Y.Y., Naima K. Yilo, Weitemeyer, K.A., Minshull, T.A., Bull, J.M., Berndt, C.,
953 2021. Porosity and free gas estimates from controlled source electromagnetic data
954 at the Scanner Pockmark in the North Sea. Submitted for publication.
955 Geotek, 2016. Multi-Sensor Core Logger - Manual.
956 https://www.geotek.co.uk/wp-content/uploads/2016/04/MSCL-manual-1-Nov-16.pdf.
957 Jackson, P.D., Smith, D.T., Stanford, P.N., 1978. Resistivity-porosity-particle
958 shape relationships for marine sands. GEOPHYSICS 43, 1250-1268.
959 10.1190/1.1440891.
960 Juhász, I., 1981. Normalised Qv - The ky to shaly sand evaluation using the
961 Waxman-Smits equation in the absence of core data, SPWLA 22nd Annual Logging
962 Symposium. Society of Petrophysicists and Well-Log Analysts, Mexico City, Mexico,
963 p. 36.
964 Karstens, J., Berndt, C., 2015. Seismic chimneys in the Southern Viking
965 Graben – Implications for palaeo fluid migration and overpressure evolution. Earth
966 and Planetary Science Letters 412, 88-100.
967 https://doi.org/10.1016/j.epsl.2014.12.017.

968 Karstens, J., Böttner, C., Edwards, M., Falcon-Suarez, I., Flohr, A., James, R.,
969 Lichtschlag, A., Maicher, D., Pheasant, I., Roche, B., Schramm, B., Wilson, M.,
970 2019. RV MARIA S. MERIAN Fahrtbericht / Cruise Report MSM78 - PERMO 2,
971 Edinburgh – Edinburgh (U.K.), 16.10. – 25.10.2018, in: Report, G. (Ed.), N. Ser. 048,
972 GEOMAR Helmholtz-Zentrum für Ozeanforschung Kiel, Kiel, Germany, p. 60.
973 https://doi.org/10.3289/geomar_rep_ns_48_2019.
974 Kim, J., Nam, M.J., Matsuoka, T., 2013. Estimation of CO_2 saturation during
975 both CO_2 drainage and imbibition processes based on both seismic velocity and
976 electrical resistivity measurements. Geophysical Journal International 195, 292-300.
977 https://doi.org/10.1093/gji/ggt232.
978 Kitamura, K., Xue, Z., Kogure, T., Nishizawa, O., 2014. The potential of Vs and
979 Vp–Vs relation for the monitoring of the change of CO_2-saturation in porous
980 sandstone. International Journal of Greenhouse Gas Control 25, 54-61.
981 http://dx.doi.org/10.1016/j.ijggc.2014.03.013.
982 Kohn, R., Vogelius, M., 1984. Determining conductivity by boundary
983 measurements. Communications on Pure and Applied Mathematics 37, 289-298.
984 https://doi.org/10.1002/cpa.3160370302.
985 Lichtschlag, A., Haeckel, M., Olierook, D., Peel, K., Flohr, A., Pearce, C.R.,
986 James, R.H., Marieni, C., Connelly, D.P., 2021. Impact of CO2 leakage from sub-
987 seabed carbon dioxide storage on sediment and porewater geochemistry.
988 International Journal of Greenhouse Gas Control This issue, Submitted for
989 publication.
990 Marín-Moreno, H., Bull, J.M., Matter, J.M., Sanderson, D.J., Roche, B.J., 2019.
991 Reactive transport modelling insights into CO_2 migration through sub-vertical fluid

992 flow structures. International Journal of Greenhouse Gas Control 86, 82-92.
993 https://doi.org/10.1016/j.ijggc.2019.04.018.
994 Marín-Moreno, H., Sahoo, S.K., Best, A.I., 2017. Theoretical modeling insights
995 into elastic wave attenuation mechanisms in marine sediments with pore-filling
996 methane hydrate. Journal of Geophysical Research: Solid Earth 122, 1835-1847.
997 https://doi.org/10.1002/2016jb013577.
998 Mavko, G., Mukerji, T., Dvorkin, J., 2009. Rock physics handbook - Tools for
999 seismic analysis in porous media. Cambridge University Press, New York.
1000 Michael, K., Golab, A., Shulakova, V., Ennis-King, J., Allinson, G., Sharma, S.,
1001 Aiken, T., 2010. Geological storage of CO_2 in saline aquifers: A review of the
1002 experience from existing storage operations. International Journal of Greenhouse
1003 Gas Control 4, 659-667. http://doi.org/10.1016/j.ijggc.2009.12.011.
1004 Mookherjee, M., Mainprice, D., 2014. Unusually large shear wave anisotropy
1005 for chlorite in subduction zone settings. Geophysical Research Letters 41, 1506-
1006 1513. https://doi.org/10.1002/2014GL059334.
1007 Muñoz-Ibáñez, A., Falcon-Suarez, I.H., Marín-Moreno, H., Martín, J.D., Mackin,
1008 P., 2019. Transport properties of saline CO_2 storage reservoirs with unconnected
1009 fractures from brine-CO_2 flow-through tests. Journal of Petroleum Science and
1010 Engineering, 106551. https://doi.org/10.1016/j.petrol.2019.106551.
1011 North, L., Best, A.I., Sothcott, J., MacGregor, L., 2013. Laboratory
1012 determination of the full electrical resistivity tensor of heterogeneous carbonate rocks
1013 at elevated pressures. Geophysical Prospecting 61, 458-470.
1014 https://doi.org/10.1111/j.1365-2478.2012.01113.x.

North, L.J., Best, A.I., 2014. Anomalous electrical resistivity anisotropy in clean reservoir sandstones. Geophysical Prospecting 62, 1315-1326. 10.1111/1365-2478.12183.

Nur, A., Mavko, G., Dvorkin, J., Galmudi, D., 1998. Critical porosity: A key to relating physical properties to porosity in rocks. The Leading Edge 17, 357-362. https://doi.org/10.1190/1.1437977.

Papageorgiou, G., Amalokwu, K., Chapman, M., 2016. Theoretical derivation of a Brie-like fluid mixing law. Geophysical Prospecting 64, 1048-1053. https://doi.org/10.1111/1365-2478.12380.

Park, J., Guillaume, S., Vöge, M., 2017. 2.5D inversion and joint interpretation of CSEM data at Sleipner CO_2 storage. Energy Procedia 114, 3989 – 3996. https://doi.org/10.3997/2214-4609.201602173.

Robinson, A.H., Callow, B., Böttner, C., Yilo, N., Provenzano, G., Falcon-Suarez, I.H., Marín-Moreno, H., Lichtschlag, A., Bayrakci, G., Gehrmann, R., Parkes, L., Roche, B., Saleem, U., Schramm, B., Waage, M., Lavayssière, A., Li, J., Jedari-Eyvazi, F., Sahoo, S., Deusner, C., Kossel, E., Minshull, T.A., Berndt, C., Bull, J.M., Dean, M., James, R.H., Chapman, M., Best, A.I., Bünz, S., Chen, B., Connelly, D.P., Elger, J., Haeckel, M., Henstock, T.J., Karstens, J., Macdonald, C., Matter, J.M., North, L., Reinardy, B., 2021. Multiscale characterisation of chimneys/pipes: Fluid escape structures within sedimentary basins. International Journal of Greenhouse Gas Control 106, 103245. https://doi.org/10.1016/j.ijggc.2020.103245.

Roche, B., Bull, J.M., Marin-Moreno, H., Leightond, T., Falcon-Suarez, I.H., White, P.R., Provenzano, G., Tholen, M., Lichtschlag, A., Lid, J., Faggetter, M., 2021. Time-lapse imaging of CO_2 migration within near-surface sediments during a

controlled sub-seabed release experiment. International Journal of Greenhouse Gas Control, Submitted for publication.

Rosas, J., Lopez, O., Missimer, T.M., Coulibaly, K.M., Dehwah, A.H.A., Sesler, K., Lujan, L.R., Mantilla, D., 2014. Determination of Hydraulic Conductivity from Grain-Size Distribution for Different Depositional Environments. Groundwater 52, 399-413. https://doi.org/10.1111/gwat.12078.

Rutqvist, J., 2012. The geomechanics of CO_2 storage in deep sedimentary formations. Geotechnical and Geological Engineering 30, 525-551. http://doi.org/10.1007/s10706-011-9491-0.

Sahoo, S.K., Madhusudhan, B.N., Marín-Moreno, H., North, L.J., Ahmed, S., Falcon-Suarez, I.H., Minshull, T.A., Best, A.I., 2018. Laboratory insights into the effect of sediment-hosted methane hydrate morphology on elastic wave velocity from time-lapse 4-D synchrotron X-ray computed tomography. Geochemistry, Geophysics, Geosystems 19, 4502– 4521. https://doi.org/10.1029/2018GC007710.

Sahoo, S.K., North, L.J., Marín-Moreno, H., Minshull, T.A., Best, A.I., 2019. Laboratory observations of frequency-dependent ultrasonic P-wave velocity and attenuation during methane hydrate formation in Berea sandstone. Geophysical Journal International 219, 713-723. https://doi.org/10.1093/gji/ggz311.

Schwalenberg, K., Gehrmann, R.A.S., Bialas, J., Rippe, D., 2020. Analysis of marine controlled source electromagnetic data for the assessment of gas hydrates in the Danube deep-sea fan, Black Sea. Marine and Petroleum Geology 122, 104650. https://doi.org/10.1016/j.marpetgeo.2020.104650.

Smeulders, D.M.J., Van Dongen, M.E.H., 1997. Wave propagation in porous media containing a dilute gas–liquid mixture: theory and experiments. Journal of Fluid Mechanics 343, 351-373. https://doi.org/10.1017/S0022112097005983.

1064 Solazzi, S.G., Hunziker, J., Caspari, E., Rubino, J.G., Favino, M., Holliger, K.,
1065 2020. Seismic signatures of fractured porous rocks: The partially saturated case.
1066 Journal of Geophysical Research: Solid Earth 125, e2020JB019960.
1067 https://doi.org/10.1029/2020jb019960.
1068 Span, R., Wagner, W., 1996. A new equation of state for carbon dioxide
1069 covering the fluid region from the triple-point temperature to 1100 K at pressures up
1070 to 800 MPa. Journal of Physical and Chemical Reference Data 25, 1509-1596.
1071 http://dx.doi.org/10.1063/1.555991.
1072 Taylor, P., Stahl, H., Vardy, M.E., Bull, J.M., Akhurst, M., Hauton, C., James,
1073 R.H., Lichtschlag, A., Long, D., Aleynik, D., Toberman, M., Naylor, M., Connelly, D.,
1074 Smith, D., Sayer, M.D.J., Widdicombe, S., Wright, I.C., Blackford, J., 2015. A novel
1075 sub-seabed CO_2 release experiment informing monitoring and impact assessment
1076 for geological carbon storage. International Journal of Greenhouse Gas Control 38,
1077 3-17. https://doi.org/10.1016/j.ijggc.2014.09.007.
1078 Thomas, E.C., 1976. The Determination of Qv From Membrane Potential
1079 Measurements on Shaly Sands. Journal of Petroleum Technology 28, 1087-1096.
1080 10.2118/5505-pa.
1081 Underschultz, J., Boreham, C., Dance, T., Stalker, L., Freifeld, B., Kirste, D.,
1082 Ennis-King, J., 2011. CO_2 storage in a depleted gas field: An overview of the
1083 CO2CRC Otway Project and initial results. International Journal of Greenhouse Gas
1084 Control 5, 922-932. https://doi.org/10.1016/j.ijggc.2011.02.009.
1085 Waage, M., Singhroha, S., Bünz, S., Planke, S., Waghorn, K.A., Bellwald, B.,
1086 2021. Feasibility of using the P-Cable high-resolution 3D seismic system in detecting
1087 and monitoring CO2 leakage. International Journal of Greenhouse Gas Control 106,
1088 103240. https://doi.org/10.1016/j.ijggc.2020.103240.

Würdemann, H., Möller, F., Kühn, M., Heidug, W., Christensen, N.P., Borm, G., Schilling, F.R., 2010. CO2SINK—From site characterisation and risk assessment to monitoring and verification: One year of operational experience with the field laboratory for CO_2 storage at Ketzin, Germany. International Journal of Greenhouse Gas Control 4, 938-951. https://doi.org/10.1016/j.ijggc.2010.08.010.

Zemke, K., Liebscher, A., Wandrey, M., 2010. Petrophysical analysis to investigate the effects of carbon dioxide storage in a subsurface saline aquifer at Ketzin, Germany (CO2SINK). International Journal of Greenhouse Gas Control 4, 990-999. https://doi.org/10.1016/j.ijggc.2010.04.008.

Zhang, Y., Nishizawa, O., Park, H., Kiyama, T., Lei, X., Xue, Z., 2017. The Pathway-Flow Relative Permeability of CO2: Measurement by Lowered Pressure Drops. Water Resources Research 53, 8626-8638. https://doi.org/10.1002/2017wr020580.